

Chapter 13

Complex Phenomena Unified Simulation Research Team

13.1 Members

Makoto Tsubokura (Team Leader)

Keiji Onishi (Researcher)

Rahul Bale (Researcher)

Koji Nishiguchi (Postdoctoral Researcher)

Kazuto Ando (Technical Staff)

Hsueh-Jui Lu (Student Trainee)

Mehdi Badri (Student Trainee)

Chung-Gang Li (Visiting Researcher)

Ryoichi Kurose (Visiting Researcher)

Tetsuro Tamura (Visiting Researcher)

Shigeru Okazawa (Visiting Researcher)

Huilai Zhang (Visiting Researcher)

Leif Niclas Jansson (Visiting Researcher)

13.2 Overview of Research Activities

The objective of our research team is to propose a unified simulation method of solving multiple partial differential equations by developing common fundamental techniques such as the effective algorithms of multi-scale phenomena or the simulation modeling for effective utilization of the massively parallel computer architecture. The target of the unified simulation is supposed to be complex and combined phenomena observed in manufacturing processes in industrial cycles. Our final goal is to contribute to enhance Japanese technological capabilities and industrial process innovation through the high-performance computing simulation.

Most of the complex flow phenomena observed in manufacturing processes are relating to or coupled with other physical or chemical phenomenon such as turbulence diffusion, structure deformation, heat transfer, electromagnetic field or chemical reaction. While computer simulations are rapidly spreading in industry as useful engineering tools, their limitations to such coupled phenomena have come to realize recently. This is because of the fact that each simulation method has been optimized to a specific phenomenon and once two or more solvers of different phenomena are coupled for such a complicated target, its computational performance is seriously degraded. This is especially true when we utilize a high-performance computer such as Fugaku. In such

a situation, in addition to the fundamental difficulty of treating different time or spatial scales, interpolation of physical quantities like pressure or velocity at the interface of two different phenomena requires additional computer costs and communications among processor cores. Different mesh topology and hence data structures among each simulation and treatment of different time or spatial scales also deteriorate single processor performance. We understand that one of the keys to solve these problems is to adopt unified structured mesh and data structure among multiple simulations for coupled phenomena. As a candidate of unified data structure for complicated and coupled phenomena, we focused on the building-cube method (BCM) proposed by Nakahashi [1].

In summary, the overview of Research Activities in FY2019 was as followings.

In the research and development of unified simulation framework 'CUBE', an empirical analysis based on the actual vehicle aerodynamic problem has been conducted. The aerodynamic drag difference was predicted for the 11 specifications of the small vehicle model, and the results showed a generally good agreement with experiment. However, there were some cases where the size was reversed. The 16 specifications of SUV type automobile models was analyzed, including the rotation conditions of tires with tread patterns. Although it showed good agreement with the experiment in general, there were cases where the tendency could not be reproduced. In the future, we plan to continue working to improve accuracy by enhancing practical know-how together with our partners.

A study of the turbulence model was conducted that is important in the empirical vehicle aerodynamic analysis, the CSM turbulence model based on the coherent structure of the flow has been implemented. Based on the results of the turbulence energy decay spectrum of the uniform isotropic turbulence, it was confirmed that accurate modeling was done. This model has already begun to be applied to practical vehicle aerodynamic analysis. We are planning to proceed further research to improve its reliability.

As a prediction verification of narrow band noise generated in automobiles, the core technologies of the CUBE compressible unified solution method has been adjusted to create an improved results. A large-scale analysis of the real vehicle model has been conducted and successfully reproduced the acoustic vibration based on acoustic feedback. In addition, the grid resolution required to capture the correct peak was found from the basic verification study, and the required calculation scale has been estimated for the future study. In the future, we plan to realize analysis with this resolution in "Fugaku" and lead to the creation of results.

The fluid-structure unified analysis method with marker particles has been modified to deal with compressible solid analysis and verification analyses were conducted. The solid stress distribution in the tensile analysis and the shear analysis of the circular plate was compared and verified with the reference solution by the finite element method. The result that the ratio of the cell size to the diameter of the circular hole was 0.78% or less showed good agreement with the reference solution. It was also confirmed that the numerical solution by this method converged to the reference solution by making the cell size finer.

In the PIC (Particle in Cell) based Euler structural analysis method, the algorithm was applied to the rigidity analysis of the vehicle white-body by increasing the calculation scale. An analysis of about 210 million cells was performed on the real vehicle model, and the Mises stress distribution at each time obtained by LS-DYNA was compared. Qualitatively valid results were obtained, and it was confirmed that the calculation turn-around time could be significantly shortened by using large-scale computational resources. In the future, based on the results obtained in this research, we will strive to create further results through the activities of the automobile consortium.

As a deployment of the unified coupled analysis method to practical problems, the dolphin-kick swimming simulation has been conducted as the field of biomechanics and realized a moving boundary fluid simulation with smooth motion. By focusing on the width of the legs and the direction of the toes, it was clarified that the direction of the toes affects the dolphin-kick movement rather than the width of the legs. In the future, we will proceed with analysis of other athletes considering the difference due to body shape, analysis with increased resolution to improve visualization of vortices. We will continue to cooperate with related research institutes toward the 2020 Tokyo Olympic Games to create results.

As an application example in the field of biomechanics, an aerodynamic simulation considering the dynamic attitude change of ski jumping has been conducted, and realized numerical fluid analysis for a series of movements from takeoff movement to initial flight movement. This is probably the world's first achievement. In the future, we plan to continue research in order to analyze different jumpers and to solve the problem of clearly explaining the causal relationship between flight distance, aerodynamic force, and flow structure.

As an application example of the unified compressible solution, a sibilant fricatives pronunciation simulation of human mouse has been conducted. As an oral cavity model, simulations were performed on both a simplified flow channel and a realistic human model. The results of the sound source spectrum showed good agreement with the benchmarks in the references. In the future, we plan to clarify the effect of complex shapes on vocalization

and proceed with research to help support denture design.

A performance evaluation and tuning of the incompressible solver has been conducted on K-computer. The performance improvement of the entire program was obtained as 2.9 times faster at 8,192 nodes than the standard numerical scheme (Multigrid + CG method) used in the incompressible framework. The speedup is suitable for creating results in “Fugaku”. It has already been confirmed that the unified solution compressible solver is expected to improve the performance by 12.8 times per node and about 25 times in total in parallel performance compared to the K-computer by the estimation of the post-K computer performance evaluation tool. In the future, we plan to evaluate scaling performance further when the number of nodes is increased and deal with the expected increase in collective communication costs.

As a basic research for constructing a flow solution method using machine learning technology, the reconstruction of a flow mode using a neural network has been tried. When the original flow field was decomposed into two modes, and reconstructed it again, the flow field could be successfully reproduced with the same accuracy as the reference. We plan to extend this method in the future and evaluate the effectiveness of this method for 3D problems.

A feasibility study based on some well-known open source code including AMReX with the aim of implementing the adaptive mesh refinement has been conducted. Some basic simulations was conducted in search of new features suitable for our code, and gained important insights in investigating the low implementation effort and missing features in the available code. In the future, we plan to continue more detailed investigations and finally consider implementing it into CUBE.

A multi-objective optimization analysis framework has been developed and a genetic-evolutionary optimization up to the 12th generation with 4-objective functions has been conducted. From the Pareto solution in the obtained aerodynamic drag (Cd) value and the difference in drag (ΔCd) to the wind direction, it was confirmed that the tendency of the objective function value was similar to the knowledge obtained in the actual design field. Furthermore, using these results as training-data, a surrogate model construction was tried by machine learning with 9 design variables as inputs and Cd and ΔCd as outputs. The Cd value was predicted almost accurately in the prediction result by machine learning compared with the actual calculation result by CFD, and it was confirmed that the constructed neural network was appropriate. In the future, we plan to introduce design variables that reproduce more detailed shapes and improve the degree of freedom, which will lead to the creation of results in “Fugaku”.

A topology optimization framework for the Lagrangian marker particle method, which is a structural analysis method for Eulerian analysis, has been developed. The topology optimization results were verified by comparing them with those of a commercial finite element structural analysis software (LS-DYNA), and the formation of an optimized shape equivalent to the previous one was confirmed. In addition, topology optimization was performed on a design domain with 10 million design variables, which covers the white body frame of an automobile, and a frame shape close to the actual shape was obtained. In the future, we will continue to carry out various basic verification examples and optimization verifications for a large number of load cases that are assumed to be real problems, as well as to improve the optimization performance through collaboration with industry.

As part of the development of an automobile engine test bed, we performed a fuel-air mixing analysis that assumed a practical usage scenario. The simulation results of the standard engine shape showed the acceptable conservation of density, pressure and temperature comparing with the theoretical result. The comparison of the different shape of the piston showed the detailed insight of the flow mechanism for the strength of the tumble and swirl inside the engine. However, the calculation condition is still under the cold flow condition. In next step, we are planning to model the combustion inside the engine and conduct direct evaluation of combustion energy efficiency. And also we have started to provide this framework to the industrial user for the evaluation of the usability of the framework. We will continue to improve practicality through the consortium activities.

As a first step of the development of the combustion system test bed, the flow simulation of the jet engine combustor was performed. It can be inferred that the simulation qualitatively resolves the injector flow, though there was a qualitative difference at downstream section between the simulation and the PIV data which does not have depth component. In the next step, we are planning to develop the fuel spraying model and the combustion model which is specifically designed for the real engine combustors. We will continue to develop the functionality to reproduce the real state of engine combustion through the consortium activities.

As an issue of the architectural consortium, verification analysis of a test bed based on a unique fluid structure coupled analysis method was performed. First, the verification analysis for basic tower structure was performed. The results of wind pressure comparison with the wind tunnel experiments showed a well agreed profile. It proves the validity of the method that we have developed as a unique fluid-structure strong coupled unified solution that combines marker particles with the Euler-type structural analysis method. Next, the numerical stability was examined by performing analysis with various conditions of prismatic structures.

The numerical instability occurred near the prisms due to the numerical calculation method of solid strain. It revealed that it requires introducing a method that can stably calculate the solid strain without depending on the velocity field. Next, we conducted a simulation of wind resistance analysis of the dome roof of a stadium structure as an application to practical problems. We could realize the considerable world's first example of solving FSI problems at a high Reynolds number over hundred million by an Eulerian FSI method. The detailed analysis of the results has not been completed; however we plan to increase the resolution of calculation mesh to try to capture smaller flow structures and deformation modes. We will continue to develop the functionality to produce the practically useful framework for the strong-coupling fluid-structure interaction, and contribute to help users to apply this method into the practical cases through the consortium activities.

By combining aerodynamic analysis with vehicle motion analysis including suspension, steering mechanism, driver's operation reaction, etc., an analysis framework that can reproduce the actual driving state has been developed. The maneuver using a hatchback type real vehicle model has been realized and analyzed. By focusing on the roll motion and the steering input by the driver, the results consistent with the reports in the human-sensory test were obtained. In the future, we plan to carry out higher-resolution analysis and improve versatility while making improvements toward the creation results of "Fugaku".

[1] Nakahashi, K., "Building-cube Method for Flow Problems with Broadband Characteristic Length," In: Armfield S., Morgan R., and Srinivas K., editors. Computational Fluid Dynamics. (Springer, 2002, 2003), pp.77-81.

13.3 Research Results and Achievements

13.3.1 Empirical analysis using unified analysis framework CUBE

13.3.1.1 Verification analysis for WLTP in vehicle aerodynamics

The WLTP (Worldwide harmonized Light vehicles Test Procedure) is an international new standard of fuel consumption test method in the automobile industry, and an evaluation test method for aerodynamic drag using computational fluid dynamics (CFD) has been established in automobile aerodynamic design. In Europe (and other member countries), a basic agreement on test methods between companies and certification agencies will be reached in 2019, and full-scale operation is expected to begin in 2020. On the other hand, in Japan, although the agreement has been obtained between companies, the situation is still in flux as the approval of the certification agency, that is the Ministry of Land, Infrastructure, Transport and Tourism, has not been obtained. It is still important for domestic automobile manufacturers to support WLTP, which expands opportunities for using CFD, they have requested us that we should continue this research activity. However, it may be a phase that requires more active lobbying to the certification agency. In this phiscal year, with the aim of further improvement of accuracy, Suzuki Motor Co., Ltd. and Nissan Motor Co., Ltd. provided us with new vehicle shapes and actual vehicle measurement data in multiple cases, and we conducted research to improve software practicality. The rate of improvement in accuracy has already slowed down, and more efforts are required for further improvement, so continuous efforts are important. In WLTP, it is expected that the aerodynamic drag measurement value by CFD is not an absolute value but only a relative value due to the specification difference. So in this research, the aerodynamic resistance difference $\Delta C_d A [m]$ due to the specification difference has been mainly evaluated.

A total of 11 specifications were analyzed for the 2-box type small vehicle model provided by Suzuki Motor Corporation. Differences in specifications include not only large spoilers, but also consideration of combinations of optional parts such as mudguards, tow-bars, and door visors. The grid resolution is arranged with a minimum of about 1.5 mm in the necessary places such as near the grill, and adjusting it between about 1.5 to 6 mm according to the part of the car body. The number of grids is about 100 million, about 15 hours using 657 nodes of K-computer in each case for unsteady calculation of 300,000 time steps (equivalent to about 3 seconds of physical time), and 32 nodes in Oakforest-PACS that took about 43 hours to calculate. In addition, we plan to reduce the calculation time further in order to improve practicality. Figure 13.1 shows an example of the time-averaged flow velocity distribution obtained. It can be confirmed that the local change in the flow around each part affects the entire flow field such as the wake of the vehicle body and the flow in the engine room, and affects the aerodynamic performance.

Figure 13.2 shows the drag difference ($\Delta C_d A$) due to the specifications of the obtained aerodynamics drag coefficient. Although the tendency is generally grasped, there are some cases where the tendency is reversed. Consideration of grid resolution dependency, aerodynamic drag accumulation graph, reproducibility of wind tunnel test, knowledge of analysis results by other commercially available software, consideration of deformation

for soft materials, CAD shape and actual vehicle shape comparison etc., the boundary conditions have been readjusted by Immersed Boundary and the turbulence model has been improved. Thus, some improvements have been obtained. However, it cannot be said that it has sufficient accuracy yet, so we plan to continue working to improve the accuracy in next year.

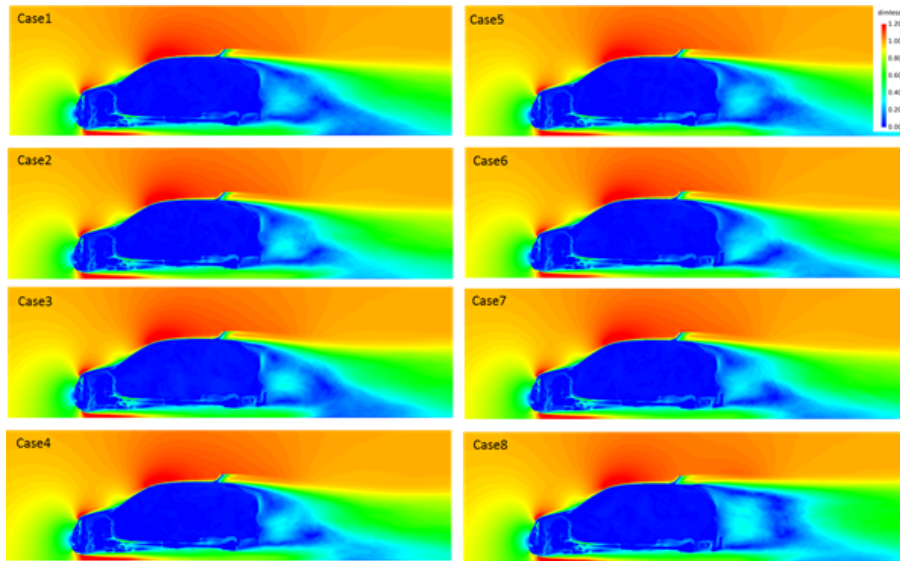


Figure 13.1: Profile of time-averaged dimensionless velocity magnitude in central section for several specifications of small vehicle simulation.

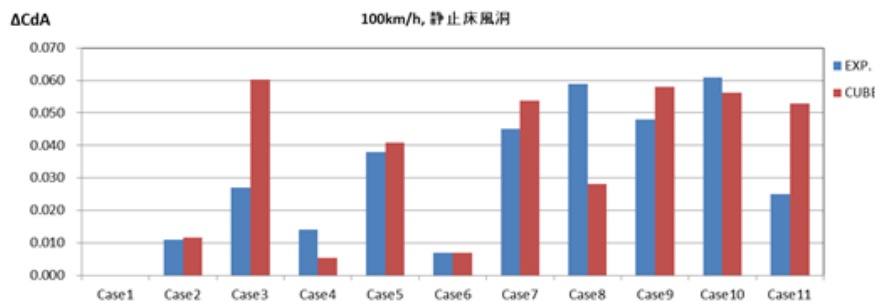


Figure 13.2: Predicted drag delta for all specifications of small vehicle simulation.

A total of 16 specifications were analyzed for the SUV type automobile model provided by Nissan Motor Co., Ltd. The actual measurement is conducted using a wind tunnel with a moving belt, and the analysis adopted that the condition involves tire/wheel rotation. Differences in specifications include a variety of aerodynamic add-on parts such as spoilers, deflectors, baffles, and grill covers. The grid resolution is adjusted to a minimum of about 1.5 mm near the grill and about 1.5 to 6 mm depending on the part of the car body. The number of analysis grids is about 120 million. Unsteady calculation of 150,000 time steps (equivalent to about 1.5 seconds of physical time) in each case required about 48 hours using Oakforest-PACS 32 nodes. Tire rotation provides a velocity boundary on the tire/wheel surface. In addition, the tire model is produced by a 3D scan technology which has the real shape, and the detailed shape including the tread pattern is reproduced. We succeeded in reproducing the rotation of the tire shape including the tread, but under this condition there are still problems that some calculations become unstable (the moment when the calculation point switches inside and outside the tire, etc.), so we will continue to improve. When this is completed, it will be the world's first case. Figure 13.3 shows an example of the time-averaged flow velocity distribution obtained. Figure 13.4 shows the difference (ΔCdA) due to the specifications of the obtained aerodynamic drag coefficient. Although

it shows good agreement with the experiment, there are cases where the tendency cannot be reproduced. In particular, since it was difficult to reproduce aerodynamic parts that affect the underfloor flow, we are reviewing the calculation conditions such as the modeling method of the wind tunnel floor surface and consideration of shape deformation. In this process, we are also preparing a group of post-treatment tools that contribute to flow evaluation, such as measuring surface pressure and creating an accumulation graph of aerodynamic drag. We will continue to work on improving accuracy in next year.

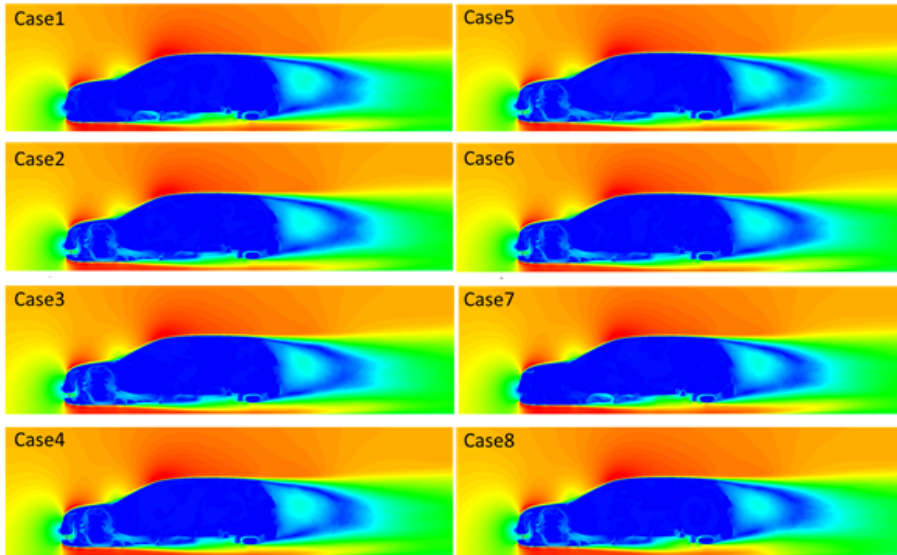


Figure 13.3: Profile of time-averaged dimensionless velocity magnitude in central section for several specifications of SUV vehicle simulation.

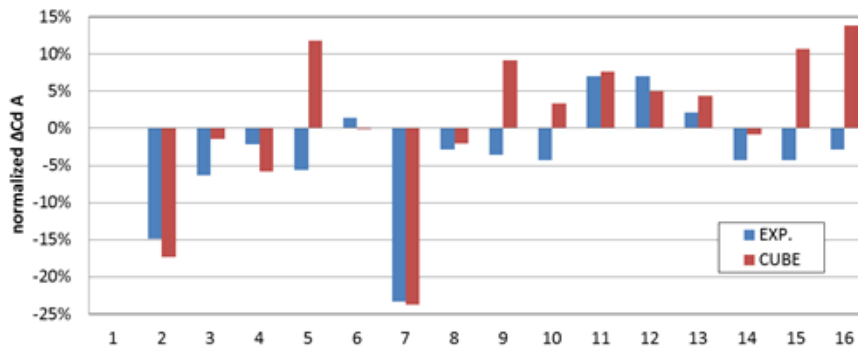


Figure 13.4: Predicted drag delta for all specifications of SUV vehicle simulation.

13.3.1.2 Narrow-band noise analysis around the engine hood of the vehicle

The narrow-band noise in automobile industries is caused by the quality problems and production issues and generally, it takes tremendous effort to solve this kind of problem in the design site. To improve the prediction accuracy, that the commercial software couldn't achieve by using the conventional methods, shorten the development period, and reduce the cost, the unified compressible solver installing in CUBE is under development. In this fiscal year, the knowhow and core technologies of the compressible solver have been summarized and the production of the results is under preparing.

For the resolution of the mesh, the finer resolution with a minimum width of 0.2 mm is located near the gap of the hood so that the acoustic feedback generated from the engine hood can be accurately captured. The total number of the grid is about 2 billion and 13,086 nodes in K-computer for about 50 hours are consumed. Figure

13.5 shows the contour of the propagation of the pressure fluctuation and the propagation with a circle shape emitting from the hood can be observed. This phenomenon is completely different from the usual acoustic noise caused by the vortex around the vehicle body. This kind of acoustic feedback can only be generated when the resonance appears. To capture this phenomenon, besides the much finer resolution compared with usual fluid simulation, a numerical scheme with extremely small dispersion and dissipation are also required. The resolution is determined by the flow velocity characteristics (the flow velocity, the gap of the hood, and the cavity length in the engine room), hence, it is necessary to perform the grid test to validate the current framework.



Figure 13.5: The propagation of the Pressure fluctuation.

In the second half of this year, because of the lack of computational resources, the large scale simulation couldn't be smoothly performed. Therefore, the basic validation of the cavity aeroacoustics problem has been conducted first. Figure 13.6 shows an example of the grid-dependent analysis of the frequency response for the simple cavity problem. From this result, the resolution required to capture the correct peak can be known, and the required computational resource can be also estimated. It can be seen that this simulation requires a resolution of around 0.5 mm (for a cavity width of 20 mm). Therefore, in the analysis equivalent to the real vehicle, it can be known that a resolution of 0.05 mm is required for the hood gap of 5 to 6 mm. In summary, 10 times of simulation time to handle the scale of the

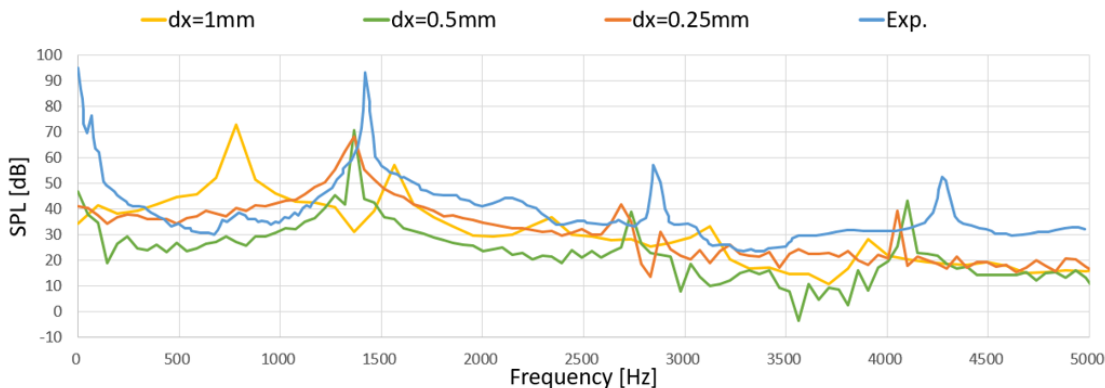


Figure 13.6: The comparison of the Frequency.

13.3.1.3 Research on turbulence models that contribute to large-scale aerodynamic analysis

In high Reynolds number turbulence analysis represented by automobile aerodynamics, it is important to select a suitable turbulence model for large-scale analysis. The Sub-grid-scale (SGS) model based on Smagorinsky (Smagorinsky, 1963) is widely used in the transient Large Eddy Simulation (LES), but it may be necessary to calculate the distance from the wall surface to the grid point (Van driest damping term of the standard Smagorinsky turbulence model). Or it requires operations that filter the model coefficients in a uniform direction to stabilize the solution (least squares operation of the dynamic Smagorinsky model [1]), and these methods has a high incidental calculation costs. In order to avoid this problem, in this study, we have mainly used the so-called “Implicit LES”, which compares the artificial viscosity introduced by the stabilization method of

the numerical scheme with the physical viscosity and we have utilized it into practical simulation cases. In this year, we implemented a coherent structure turbulence model (CSM) based on the dominant vortical flow structures, which was derived by Kobayashi et al.[2]. In this model, in modeling vortex viscosity, the local constants of the Smagorinsky SGS model are dynamically determined based on the relationship between the second invariant of the velocity gradient tensor and the energy dissipation rate of the vortex. Unlike the dynamic Smagorinsky model, it does not require filtering and does not require distance calculation, which is advantageous for large-scale calculation and application to complicated shapes. The SGS model by Smagorinsky is expressed as follows:

$$\nu_t = C\bar{\Delta}^2|\bar{\mathbf{S}}|, \quad |\bar{\mathbf{S}}| = \sqrt{\bar{S}_{ij}\bar{S}_{ij}},$$

where $\bar{\Delta} = (\bar{\Delta}_1\bar{\Delta}_2\bar{\Delta}_3)^{1/3}$ is the filter width, given by the grid width $\bar{\Delta}_i$ in the i -th direction. In the CSM, the model coefficient C is determined as follows. The second invariant of the velocity gradient tensor Q is represented as:

$$Q = \frac{1}{2}(W_{ij}W_{ij} - S_{ij}S_{ij}),$$

$$\bar{\mathbf{W}} = \frac{1}{2}(\nabla\bar{\mathbf{u}} - (\nabla\bar{\mathbf{u}})^T), \quad |\bar{\mathbf{W}}| = \sqrt{\bar{W}_{ij}\bar{W}_{ij}},$$

where $\bar{\mathbf{W}}$ is the vorticity tensor. This definition is termed the Q-criterion, and it is often used to visualize vortex structures [3]. Kobayashi determined the model coefficients (in non-rotating flow) independently of the flow properties and Reynolds number, as follows:

$$F_{CS} = Q/E,$$

$$E = \frac{1}{2}(W_{ij}W_{ij} + S_{ij}S_{ij}),$$

$$C = C_1|F_{CS}|^{3/2}, \quad C_1 = 1/20.$$

As a result, an eddy viscosity model is expressed, in which the coefficient is automatically zero in laminar flow, and is naturally damped in the wall direction. For details, refer to [2].

Figure 13.7 shows the basic verification results for this turbulence model on the isotropic turbulence decay energy spectrum. The homogeneous incompressible isotropic turbulence was generated in a three-dimensional cubic box using the random Fourier mode. The side length of the box was $L = 0.09 \times 2\pi m$, with a number of grid (cell) of $128 \times 128 \times 128$ in three dimensions. The number of Fourier modes was 5000 and a generic dynamic viscosity $\nu = 1.0 \times 10^{-5} m^2/s$ was chosen. The initial turbulence velocity field was generated from the energy spectrum table of Comte-Bellot et al. (CBC) [4], based on the method of Saad et al. [5]. A Fourier series of an arbitrary spatial velocity field u at point x is given by:

$$\mathbf{u}(\mathbf{x}) = 2 \sum_{m=1}^M q_m \cos(\kappa_m \hat{\mathbf{k}}_m \cdot \mathbf{x} + \psi_m) \hat{\boldsymbol{\sigma}}_m,$$

where M is the number of modes, q_m is the amplitude, κ_m is the m -th wavenumber, and $\hat{\mathbf{k}}_m \equiv (k_{x,m}, k_{y,m}, k_{z,m})$ is a unit direction vector. The procedure consisted of choosing random $\hat{\mathbf{k}}_m$ and ψ_m with q_m obtained from the energy spectrum such that $q_m = \sqrt{E(\kappa_m)\Delta\kappa}$. The modal direction vector $\hat{\boldsymbol{\sigma}}_m$ was evaluated enforcing the divergence-free constraint; it was selected to be orthogonal to $\hat{\mathbf{k}}_m$,

$$\hat{\mathbf{k}}_m \cdot \hat{\boldsymbol{\sigma}}_m = 0, \quad \forall m \in \{0, 1, \dots, M\}.$$

In Fig. 13.7, the input spectrum corresponds to the CBC data (solid lines). The simulated data are shown in filled circles and correspond to non-dimensional times of $t^* = 42, 98, 171$, respectively. The Nyquist limit is indicated via the vertical dashed line. The results of the initial spectrum and the decaying spectrum both well reproduced the results of the direct numerical simulation, confirming that accurate modeling was performed.

This model has already begun to be applied to practical vehicle aerodynamic analysis. From the results of initial studies, it has been confirmed that reasonable results with more suppressed numerical viscosity can be shown in areas that were previously sensitive to flow separation. In the next step, we plan to continue research to improve reliability by implementing a wide range of verification calculations and accumulating empirical calculation experiences.

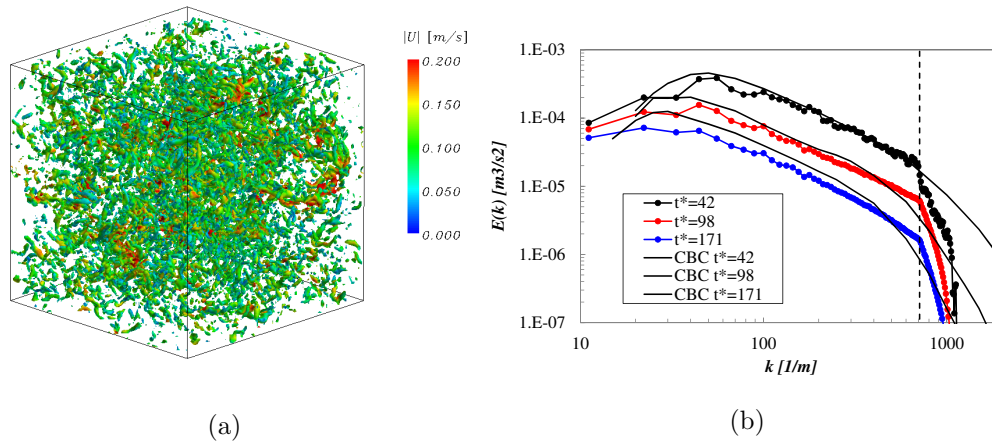


Figure 13.7: Isotropic turbulence decay energy spectrum for the CSM turbulence model. (a) The turbulence structures visualized by the Q-criterion. (b) The black circle represents the initial reference energy $E(k)$ for each wavenumber k ; the red or blue colored circle shows simulation result. The solid line shows CBC data. The Nyquist limit is indicated via the vertical dashed line.

13.3.1.4 References

- [1] M. Germano, U. Piomelli, P. Moin, W. H. Cabot, A dynamic subgrid-scale eddy viscosity model, *Physics of Fluids A: Fluid Dynamics* 3 (7), (1991), 1760-1765.
- [2] H. Kobayashi, The subgrid-scale models based on coherent structures for rotating homogeneous turbulence and turbulent channel flow, *Physics of Fluids* 17 (4), (2005), 045104.
- [3] M. Tanaka, S. Kida, Characterization of vortex tubes and sheets, *Physics of Fluids A: Fluid Dynamics* 5 (9), (1993), 2079-2082.
- [4] G. Comte-Bellot, S. Corrsin, Simple Eulerian time correlation of full-and narrow-band velocity signals in grid-generated “isotropic” turbulence, *Journal of Fluid Mechanics* 48 (2), (1971), 273-337.
- [5] T. Saad, D. Cline, R. Stoll, J. C. Sutherland, Scalable Tools for Generating Synthetic Isotropic Turbulence with Arbitrary Spectra, *AIAA Journal* 55 (1), (2017), 327-331.

13.3.2 Verification analysis of Eulerian finite volume formulation using Lagrangian marker particles for compressible solid

13.3.2.1 Development of Eulerian finite volume formulation using Lagrangian marker particles for compressible solid analysis

In this study, in order to deal with large-scale structural analysis problems that reproduce complex shapes that are difficult to calculate with conventional methods, the Eulerian fluid-structure unified analysis method using Lagrangian marker particles has been developed. In this fiscal year, to deal with structural analysis problems with compressible materials, improvement of the fluid-structure unified analysis method with marker particles and implementation of an Eulerian finite volume formulation using Lagrangian marker particles for compressible solid analysis has been conducted. At this time, the conservation of mass and the equation of motion of compressible materials are expressed by the following equations [1].

$$\rho J = \rho_0$$

$$\rho \left\{ \frac{\partial \mathbf{v}}{\partial t} + (\mathbf{v} \cdot \nabla) \mathbf{v} \right\} = \nabla \cdot \boldsymbol{\sigma} + \rho \mathbf{b}$$

Here, ρ_0 is the mass density at initial condition, ρ is the mass density, J is the volume ratio, \mathbf{v} is the velocity, σ is the Cauchy stress, and \mathbf{b} is the body force. In this study, the solid is modeled as a compressible neo-Hookean solid and the constitutive equation is given by [2]

$$\boldsymbol{\sigma} = J^{-5/3}G \left\{ \mathbf{B} - \frac{1}{3} (\text{tr}\mathbf{B}) \mathbf{I} \right\} + K (J - 1) \mathbf{I},$$

where, G is the shear modulus, \mathbf{B} is the left Cauchy-Green deformation tensor, \mathbf{I} is a second-order unit tensor, and K is the bulk modulus.

In order to confirm the validity of the proposed method, the tensile analysis and the shear analysis of a flat plate with a circular hole were conducted and the solid stress distribution is compared with the reference solution obtained by the finite element method. Furthermore, by verifying the stress distribution when the mesh resolution is changed, the mesh resolution required to obtain the desired accuracy is clarified. In the following examples, the structure has Young's modulus and mass density of the steel, and the void region is given $\rho_0 = 1.0\text{kg/m}^3$ to avoid numerical instability. The height of the flat plate(structure) is 1.0 m and the width is 0.5 m, and a circular hole with a diameter of 0.25 m is arranged in the center of the flat plate. The length of the plate in the direction perpendicular to the paper surface (y-direction) is assumed to be a unit length, and the plane strain state is assumed by setting the velocity in the y-direction to zero.

13.3.2.2 Verification analysis by the tensile analysis and the shear analysis of a flat plate with a circular hole

The lower end of the flat plate fixes the velocity component in all directions to zero, and the upper end of the flat plate gives a tensile velocity that increases linearly in the time direction in the positive z-axis direction. No restraint conditions are given to the other end faces. In the proposed method, the above velocity boundary conditions are given by the marker particles arranged in the region. In this example, the analysis time is up to 1 ms. Therefore, the displacement of the upper end of the flat plate is $1 \mu\text{m}$, and this example can be regarded as a minute deformation problem. In the calculation by the proposed method, the time increment size is set so that the CFL number for the stress wave velocity is 0.1874 at each spatial resolution. In order to obtain the reference solution, a sufficiently fine finite element mesh is used, and the finite element size of the orthogonally divided region excluding the circumference of the circular hole is $1/640$ m.

Figure 13.8 shows the reference solution at $t = 1$ ms, the marker particles at each spatial resolution, and their Mises stress distribution. In this calculation, the number of marker particles in one cell is fixed at 2×2 . The result that the ratio of the cell size to the diameter of the hole is 0.78% or less shows good agreement with the reference solution, and it can be seen that the stress concentration at the upper part and the lower part of the hole is particularly reproduced. In addition, in order to quantitatively verify the validity of the numerical solution, the time history of strain energy is compared with the reference solution. As shown in Figure 13.9, it can be confirmed that the numerical solution by this method converges to the reference solution by making the cell size h finer. In addition, Figure 13.10 shows the error ϵ of the strain energy with respect to the reference solution at $t = 1$ ms and its spatial convergence. It is confirmed that the error converges at the order of 0.025 and that the error is 0.27% at the cell size $h = 1/1024$ m.

13.3.2.3 Verification analysis by shear analysis of a flat plate with a circular hole

The analysis conditions are the same as the example in the previous section, except that the upper end of the flat plate is given a shear rate that increases linearly in the time direction in the positive x-axis direction. Figure 13.11 shows the reference solution at $t = 1$ ms, the marker particles at each spatial resolution, and their Mises stress distribution. The result that the ratio of the cell size to the diameter of the hole is 0.78% or less shows a good agreement with the reference solution, and it can be seen that the stress concentration around the hole is particularly reproduced. From Figure 13.12, it can be confirmed that the numerical solution by the proposed method converges to the reference solution by making the cell size h finer. Furthermore, Figure 13.10 also shows the error of strain energy with respect to the reference solution at $t = 1$ ms and its spatial convergence. It is confirmed that the error converges at the order of 0.077 and that the error is 0.17% at the cell size $h = 1/1024$ m.

When the ratio of the cell size to the diameter of the circular hole is 1.56% or more, it can be seen that the oscillation of stress occurs at the top corners of the flat plate in Figure 13.8 and Figure 13.11. This is because the velocity field is discontinuous between the cell to which the velocity boundary condition is given and the cells around it. Thus, the velocity gradient calculated from the velocity of these cells is overestimated.

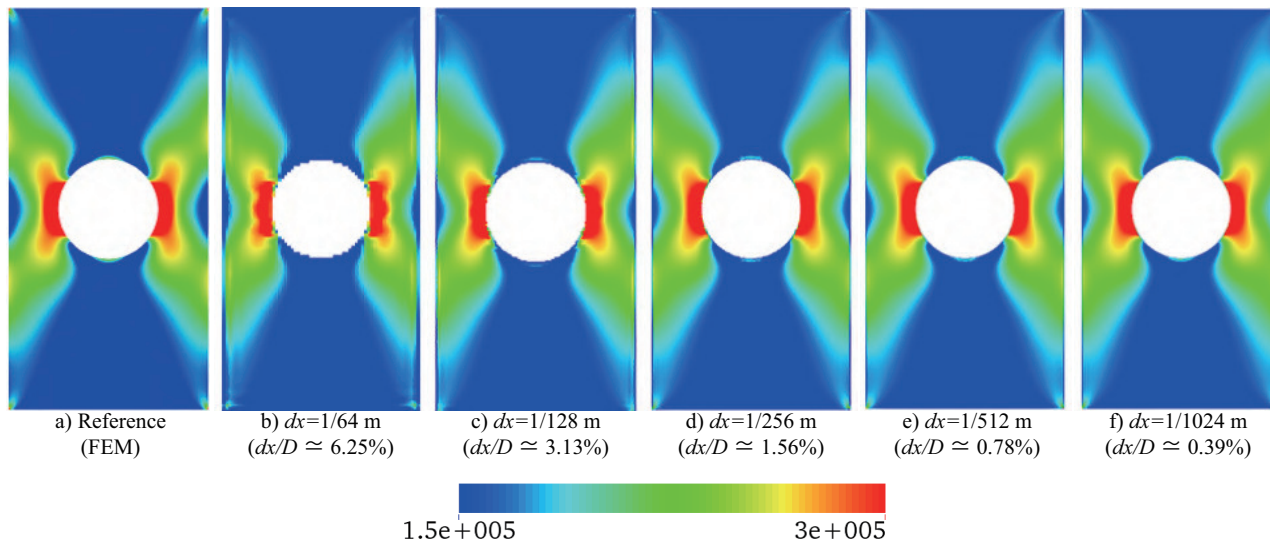


Figure 13.8: Tensile deformation problem of a flat plate with a circular hole: Distribution of Marker particles and their Mises stress distribution at $t = 1\text{ms}$.

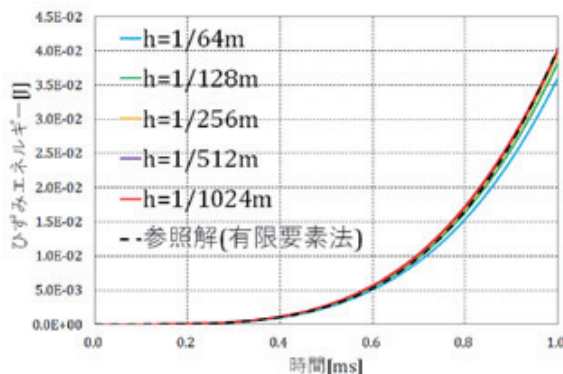


Figure 13.9: Tensile deformation problem of a flat plate with a circular hole: Time history of strain energy.

In order to avoid this numerical oscillation even when the spatial resolution is low, it is necessary to introduce a calculation method for solid deformation tensors that does not require velocity gradient calculation and we continue to work on development to improve analysis accuracy.

13.3.2.4 Large-scale real vehicle model structure analysis using Euler structure analysis framework

In this research, in order to conduct a large-scale structural analysis that reproduces detailed shapes of real vehicle model that are difficult to calculate with conventional methods, we are developing a unique fluid-structure unified solution method that combines an Euler-type structural analysis method with marker particles. We applied the algorithm to the stiffness analysis of the vehicle white-body by increasing the scale of calculation. In this report, steel is assumed as the solid material in all the numerical analysis examples, and $\rho = 7850\text{kg/m}^3$, $E = 200\text{GPa}$, $\mu = 0.3$ are given as the material parameters of the solid. Here, E is Young’s modulus and μ is Poisson’s ratio. In the region where no solid exists, $\rho = 1.0\text{kg/m}^3$ is set to avoid zero division in numerical calculation. The shape of the automobile body and the hierarchical Cartesian grid based on the building cube method are shown in Fig. 13.13. The minimum cell size was 1.86 mm, and the total number of cells was about 210 million. $32 \times 32 \times 32$ cells are evenly spaced in a cube. As shown in Fig. 13.14, the boundary conditions in the torsional stiffness test are reproduced by setting the velocity for the marker particles shown in red. The two marker particle groups at the rear of the vehicle body are completely fixed, and the two marker particle groups

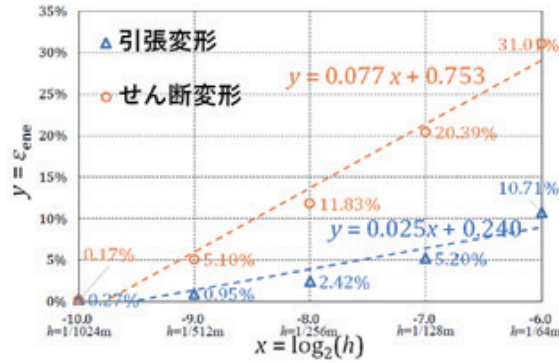


Figure 13.10: Error of strain energy at $t = 1\text{ms}$ with respect to reference solution (finite element method) and its spatial convergence.

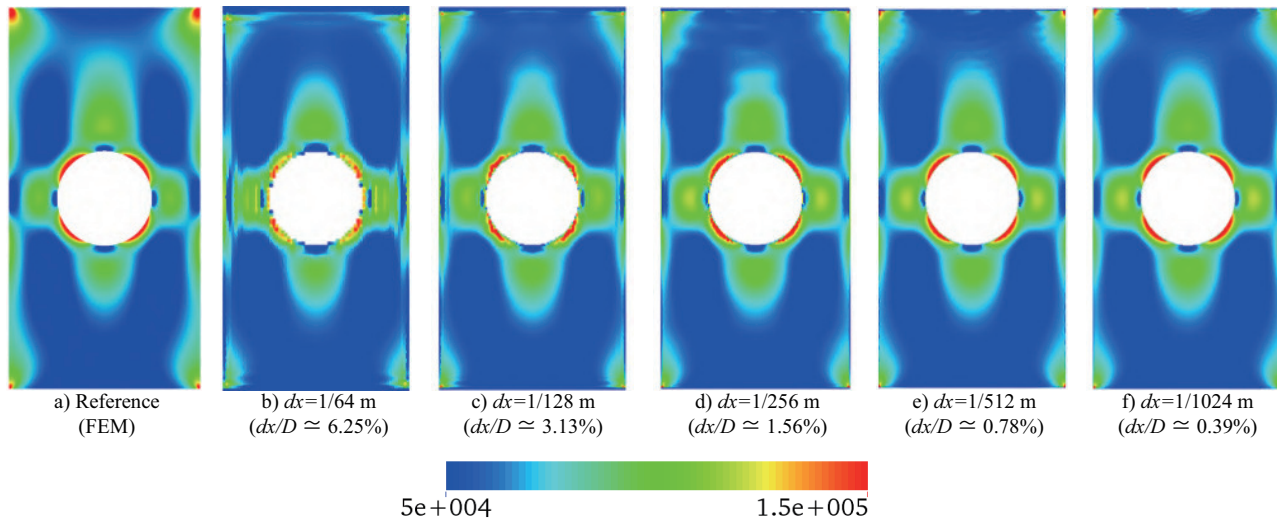


Figure 13.11: Shear deformation problem of a flat plate with a circular hole: Distribution of Marker Particle and its Mises Stress Distribution at $t = 1\text{ms}$.

at the front of the vehicle body give a velocity that increases linearly in the positive and negative directions of the z -axis. In this example, the time increment was set to $6.25 \times 10^{-5}\text{ms}$, and calculations were performed up to 4800 steps ($t = 3.0\text{ms}$). 13,065 nodes of K-computer were used for this calculation. In order to compare and verify the numerical solutions by the proposed method, the reference solution was calculated using the commercial solid-structure analysis code LS-DYNA. The total number of elements of the finite element mesh in LS-DYNA was about 660,000, and it is consisted with about 580,000 shell elements, about 10,000 solid elements, 14 beam elements, and about 70,000 rigid body elements.

Figure 13.15 shows the Mises stress distribution at each time obtained by the proposed method and LS-DYNA. However, the color bar of Mises stress is normalized. From these figures, it could be confirmed that the Mises stress distribution obtained by the proposed method is qualitatively generally valid. Table.13.1 shows the turn-around time of the proposed method and LS-DYNA. The turn-around time could be significantly shortened in the calculation by the proposed method by using a large-scale computational resource (K-computer 13065 node \times 2.4 hours). In the future, based on the results obtained in this research, we will continue to create further results through the activities of the automobile consortium organized by RIKEN.

13.3.2.5 References

[1] G. A. Holzapfel, "Nonlinear Solid Mechanics: A Continuum Approach for Engineering," Wiley, 2000.
 [2] R. W. Ogden, "Non-linear elastic deformations," Courier Corporation, 1997.

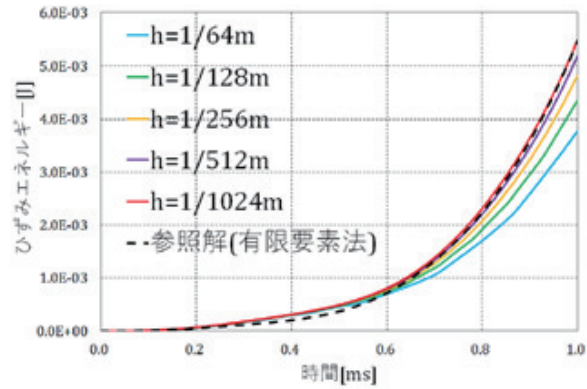


Figure 13.12: Shear deformation problem of a flat plate with a circular hole: Time history of strain energy.

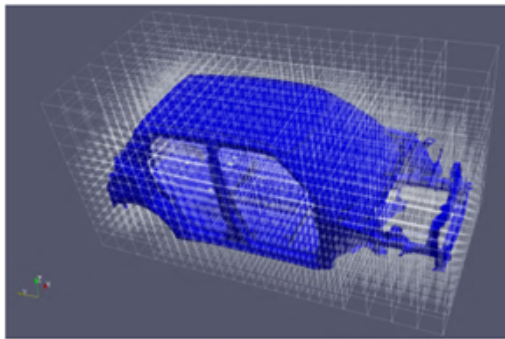


Figure 13.13: Overview of Euler grid and vehicle white body shape (finest size: 1.86mm, number of grids 210 million).

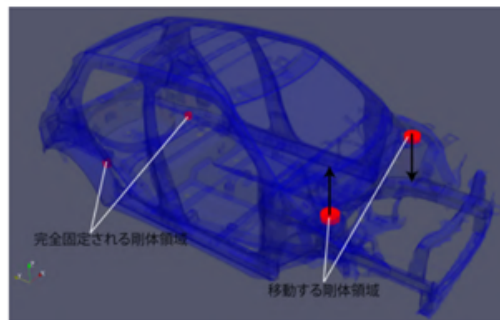


Figure 13.14: Geometric boundary conditions: (red) velocity boundary on a jig given by marker particles.

Table 13.1: Turn-around time comparison

	LS-DYNA	Proposed method
Grid generation	several weeks	10 minutes
Calculation	0.75 hours	2.4 hours
Visualization	1 hour	1 hour
Total (Turn-around time)	several weeks	3.6 hour

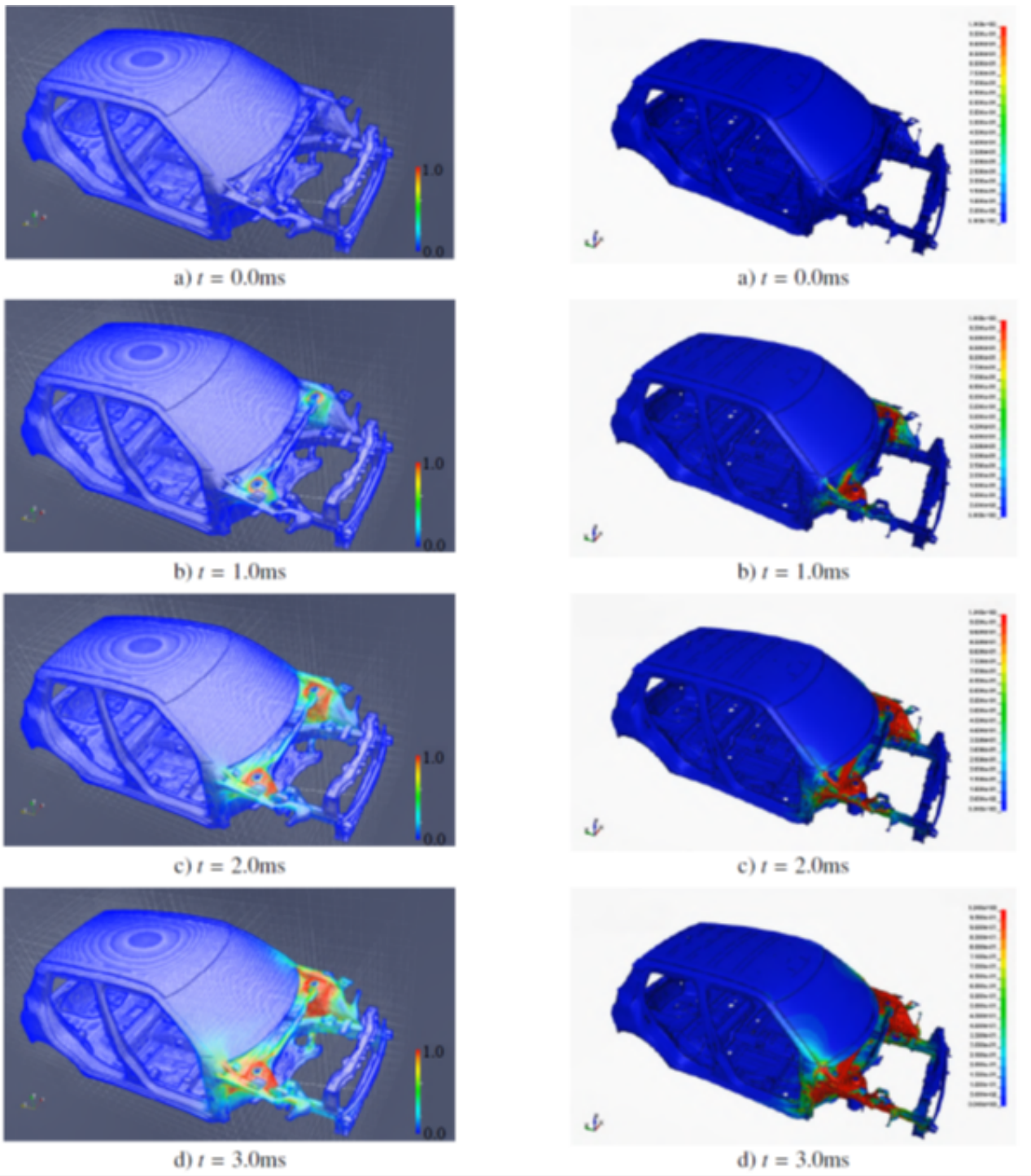


Figure 13.15: Analysis results by CUBE (left) and LS-DYNA (right) (Mises stress distribution).

13.3.3 Biomechanics CFD–Development of unified coupled analysis methods into practical problems

13.3.3.1 Role of feet orientation on thrust generation in dolphin-kick swimming

In swimming competitions using the 50m pool, under water swimming is permitted up to 15m from the starting point and after turning back all swimming styles other than breaststroke. Generally, the swimming style employed for underwater swimming is known as dolphin kick. As a result, there is much interest in optimizing the swimming performance of the dolphin kick swimming.

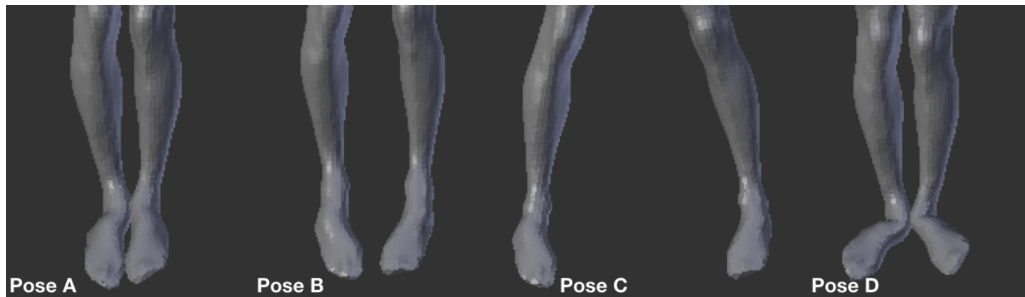


Figure 13.16: The four feet orientations considered in this study.

Since it is difficult to measure the fluid forces generated unsteady swimming such as dolphin kick swimming experimentally, various studies using computational fluid dynamics have been conducted. The results of such studies suggest that lower limbs and feet account for major contribution to the propulsive forces, and that the joint angle of the lower body is important. However, most of the prior studies focus on a standard orientation of the legs and feet. Therefore, in this study, we investigate the role of feet orientation on the propulsive forces in dolphin kick swimming using numerical simulations. For that purpose, the position of the legs such as the width of the legs and the direction of the ankles was changed variously using the body shape data of the athlete measured using the 3D scanner. Experimentally obtained dolphin-kick motion was employed of the simulations. The movement of the lower body was converted into coordinates and given as motion data. The CAD model of the swimmer’s body was coupled with the motion capture data to generate CAD model based motion model.

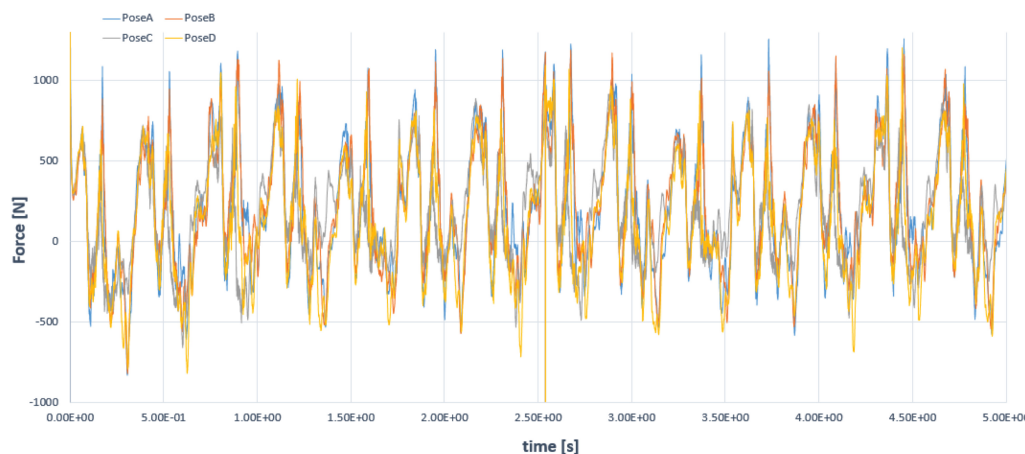


Figure 13.17: Instantaneous thrust generated by the four feet poses.

Numerical simulation was carried out using this setup for four different feet orientations, the results of which are shown in Fig.13.16. From the results of these simulations we find that there are differences in the flow velocity distribution, the vortex structure generated on the sole of the foot when the leg is kicked down, and the flow velocity vector. By comparing these results focusing on the width of the legs and the direction of the toes, it was confirmed that the direction of the toes rather than the width of the legs affects the diving

Table 13.2: Comparison of averaged thrust produced by the four feet orientations.

Pose	A	B	C	D
Thrust (N)	213	220	181	134

method movement. It was confirmed that collecting the flow velocity vectors generated on the sole of the foot more centrally and posteriorly with the toes facing the center has a large effect on propulsive forces.

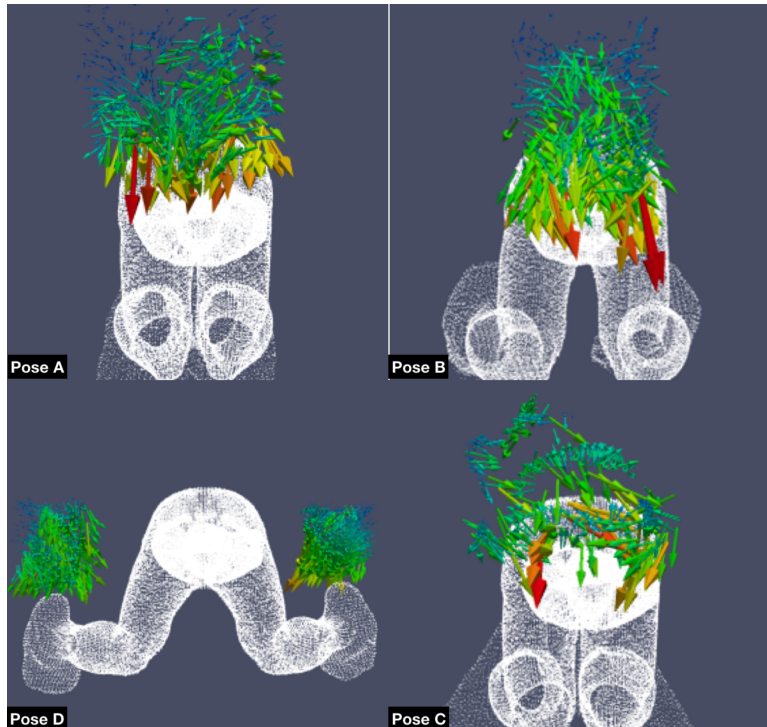


Figure 13.18: Visualization of the flow around the feet at the end of the power stroke.

Next, the thrust generated by the swimmer is plotted compared in Fig.13.17. The vertical axis is the force of the swimmer, and the horizontal axis is the time. For each leg orientation, the red circled area where the swimmer has the most propulsion. From the figure, it can be seen that Pose A and Pose B produce more thrust on average compared to the other two feet orientations. The time averaged thrust generated by each of the four feet orientations are shown in Table. 13.2.

PoseB has the most propulsion power, and PoseA also has a value close to PoseB, but PoseC and PoseD have relatively low values, and PoseD has the lowest propulsion power. From Fig.13.18, it can be seen that the flow velocity vector is generated in a circle on the sole of the foot.

In summary, we simulated the diving movement by intentionally changing the leg position for one athlete, and compared the effect of the leg position on the propulsive force. The following findings were obtained from the simulation results.

1. There was a difference in the flow velocity distribution and the force generated by the swimmer depending on the position of the legs.
2. The magnitude of the vorticity generated on the sole of the foot when the leg was kicked down greatly differed depending on the width of the leg opening and the direction of the toe.
3. There was a correlation between the vortex generated on the sole of the foot and the magnitude of the flow velocity vector.
4. The direction of the toes had the greatest effect on propulsion, followed by the width of the legs that had the greatest effect on propulsion.

From the above, it is considered that the position of the legs in the diving swimming method can be more propulsive by the posture in which the legs are closed and the toes are aligned with each other as in Pose B. In optimizing the diving method, as a future research subject, it is necessary to consider the difference due to body shape, perform the same analysis for other athletes, and perform more precise analysis with increased resolution to improve the visualization of vortices.

13.3.3.2 Aerodynamic simulation of the dynamic flight posture in ski jumping

In ski jumping competitions, take-off and flight posture are important movements that are greatly influence the flight distance. These two postures are closely related, and errors in the take off posture will adversely affect the flight posture and it is usually quite difficult to make adjustments during the flight. On the other hand, a jumper must dynamically adjust the flight posture taking into account the wind condition to prevent the increase in drag and the decrease in lift as much as possible. Failure to do so can result in the jumper stalling mid-flight, greatly reducing the jumping distance. Although these two movements are very important, there has been no study that aerodynamically investigated both movements together. This is because it is difficult to continuously reproduce both movements in a wind tunnel experiment, and it is also difficult to reproduce a large flight posture change in simulations that employ unstructured grid that that is typically used for such analysis. However, with the advent of local mesh refinement techniques in cartesian meshes and immersed boundary methods that can faithfully reproduce the dynamic motion of a ski-jump, for example, it is now possible to carryout such simulations. Therefore, the purpose of this study is to carry out aerodynamic simulation using the above framework for take-off motion to initial flight motion, and to investigate the characteristics of the aerodynamic force on the jumper. In this study, in order to reproduce more detailed movements before analysis, we asked for the cooperation of an active ski jumper and attached a motion sensor to the jumper to measure posture change data. In addition, a GPS device was attached to the jumper to measure the flight trajectory and instantaneous speed. Using these data, aerodynamic simulations were performed for movements from 0.3 seconds before takeoff to 0.7 seconds after takeoff.

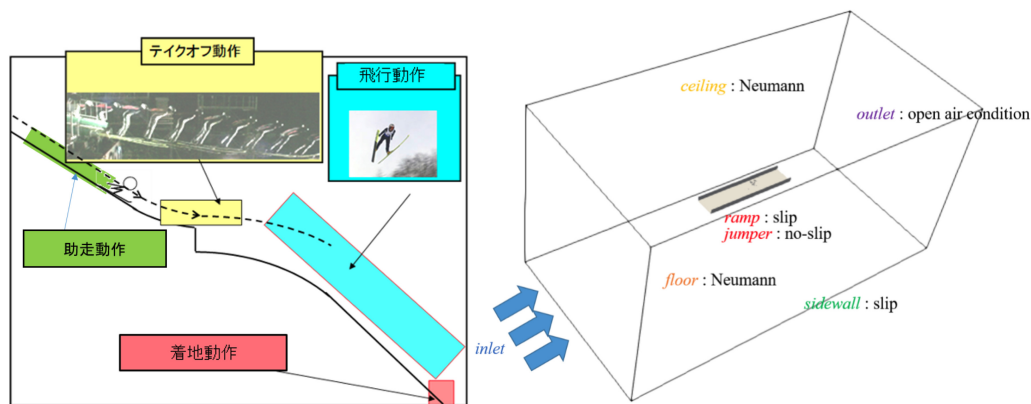


Figure 13.19: (Left) Schematic of ski jump. (Right) Computational domain setup.

The ski jumping competition is one of the Nordic skiing competitions held in the stadium, and is competed in two elements: distance and beauty of flying type. In ski jumping competitions, a series of movements can be classified into six categories: run-up, take-off, initial flight, stable flight, landing preparation, and landing (Fig.13.19). Of these movements, two important elements for extending the flight distance are take-off and flight posture (initial flight / stable flight). In the take-off motion, while maintaining the speed close to 90 m / s obtained during the approach run, the posture is changed significantly from the crouched position to the flight posture within a very short span of time, from 0.2 to 0.3 s. This movement, which involves a large change in posture in a short period of time, is considered to be a very difficult and important movement. In flight, jumper takes a posture to obtain a large lift and low drag. Although there is no significant change in posture during flight, it is necessary to fine-tune the posture taking into consideration of the wind conditions. In ski jumping competitions, once a stall occurs during flight, it is difficult to extend the flight distance, so stall prevention is also very important.

Table 13.3 shows the start gate, flight distance, Run time, and flight time of each trial measured in this

Table 13.3: Information obtained in each jump.

	Starting Gate	Flying Distance (m)	Run time (s)	Flight time (s)
First jump	26	112	6.1	4.2
Second Jump	17	90	5.7	3.2
Third Jump	22	113	5.8	4.1

study. In the measurement in this study, the largest gate is No. 26 and the smallest gate is No. 17, so there is a difference of 4.5 m in the maximum approach distance. In this study, the boundary conditions were set as shown in Fig.13.19.

From Fig. 13.20, in the first attempt, there was no significant increase in drag immediately after takeoff (around 0 s at time), which was seen in other attempts, and the drag decreased significantly between 0.3 s and 0.4 s after that. On the other hand, in the 2nd and 3rd trials, the drag increases immediately after the takeoff, then decreases and increases once, and then decreases again. At around 0.7 s time, there was no big difference between each attempt.

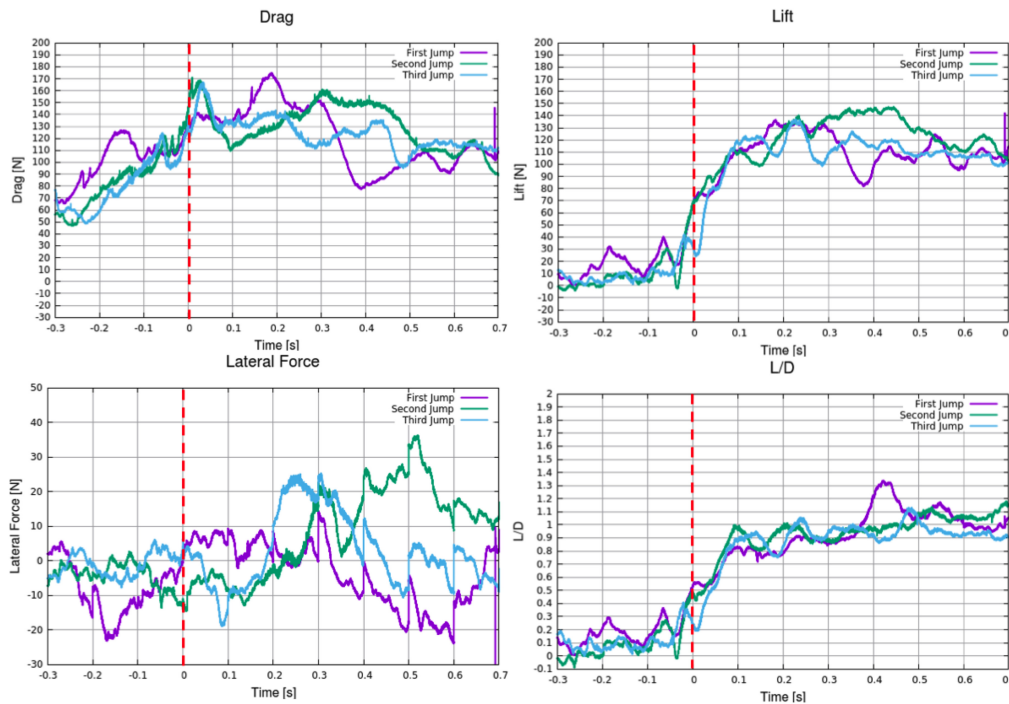


Figure 13.20: Evolution of drag, lift, lateral force and lift-drag ratio.

First, as with drag, lift has a low value before takeoff (before time 0 s) and tends to increase significantly by taking a flight attitude after takeoff (after time 0 s). However, in the first attempt, the lift was very high at time -0.2 s, and a fall similar to drag was seen at time 0.3 s to 0.4 s. On the other hand, it can be seen that in the second attempt, unlike the other attempts, the high value was maintained between the times of 0.3 s and 0.5 s. In the third attempt, there was no significant decrease after takeoff, but as with drag, it continued to decrease gradually. At 0.7 s, as with drag, there was no significant difference in lift between the three attempts. The lift to drag ratio is defined by the following equation.

$$L/D = \frac{\text{Lift}}{\text{Drag}} \quad (13.1)$$

Regarding the time transition of the lift-drag ratio, for each attempt, the value was close to 0 before the takeoff (before time 0 s), and after take-off L/D rapidly increases from 0 to 1 within a span of 0.1 s. As for the difference between the trials, it can be seen that the lift-drag ratio increases significantly only in the first run at around 0.4 s. A snapshot of the streamlines of the flow at 0.6s after take-off is presented in Fig.13.21.

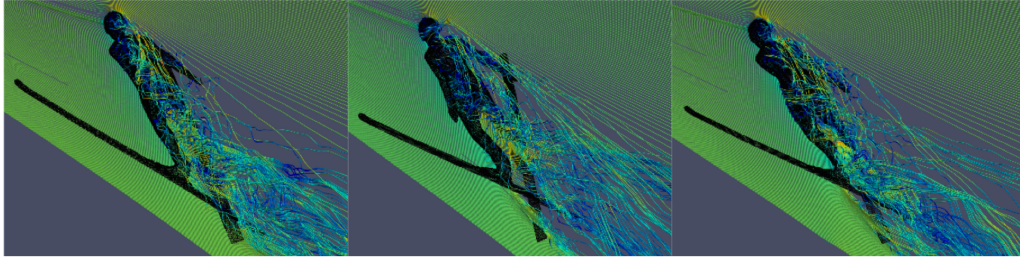


Figure 13.21: Streamlines at $t = 0.6s$ for first, second and third jump, respectively.

13.3.3.3 Sibilant fricatives pronunciation simulation using a unified compressible solution

The simulation of human speech organ contributes to the dental application. For example, a well-designed denture enables patients speak better, especially improvement in pronouncing words containing sibilants or fricatives. However, human phonation process is a tough objective for the simulation because the fluctuation pressure which generates the sound is much smaller compare with the atmospheric pressure. Specifically, the amplitude of sound wave is only 0.01% of standard atmosphere. That means the simulation system is sensitive to the accuracy of the numerical scheme. Therefore, a numerical framework which is suitable for high-performance computing is built for modelling the sibilant fricative production in this study.

The implicit time scheme with immersed boundary method based on a hierarchical structure grid as well as the modified solution-limited time stepping method for the compressible flow are adopted. Firstly, the acoustic resonance generated from the flow around the single plate is simulated to validate the numerical scheme and the result shows that this framework is highly efficient and suitable for the massive parallelization system to tremendously save the calculation time. Then, the simulation for a simplified model of the sibilant /s/ is conducted and SPL profiles are in good agreement with the experimental results. Finally, the simulation for a realistic geometry of sibilant /s/ scanned from the human vocal tract is performed to demonstrate that this framework is capable of making a contribution to the dental application, such as helping designing the dental prosthesis.

The LUSGS implicit algorithm and the Unified Time Stepping scheme are applied for the time advancement. The Roe scheme with 5th order MUSCL is used to approximate the convective terms. And the second order central difference method is adopted to calculate the magnitudes of the viscous terms. The absorbing boundary condition is used at the outlet for avoiding the computational domain being polluted by the reflecting pressure waves. The immersed boundary method with the hierarchical structured grid is used to simulate the complex geometry surface. And the OpenMP and MPI are applied for parallel computation.

The resonance plays an important role in acoustics simulation, since it enhances the amplitude of sound wave and makes characteristics of sound clearly. Hence, the model of single plate is simulated to check the phenomenon of resonance with the benchmark [1] by present framework. In Fig. 13.22, the fluctuation pressure is indicated. The resonance occurs in a half-wavelength mode along the plate length at $U = 44m/s$, both of the wave length and intensity of the sound wave can be observed.

The sibilant fricative is the common consonant in each language produced by forcing air through a narrow channel inside the oral cavity. Nozaki et al. [2] replicated a realistic model of a subject pronouncing /s/ and used incompressible solver to simulate the flow field. Yoshinaga et al. [3] simulated the simplified sibilant fricatives model to investigate the mechanisms of the production process in the vocal tract. Both the simplified and realistic model are selected to be the validation by present framework. Fig. 13.23 is the instantaneous velocity magnitude. Observably, the flow is accelerated at the narrow channel and the turbulence is caused when the flow goes through the channel. As shown in Fig. 13.23, the sound source locates around the gap before the exit, which is the high RMS value region. The fluctuation pressure out of the oral cavity is shown in Fig. 13.24, the frequency of this sound wave is about 5kHz. The SPL spectrum sampling at 10 cm far from the exit of oral cavity is shown as Fig. 13.25. The result simulated by current framework has good agreement with the benchmark after 5kHz which is the first characteristic peak. Moreover, Fig. 13.26 is the instantaneous velocity of realistic model. Clearly, the flow is speed-up between the articulators, and then products the sound by turbulence. Besides, the SPL spectrum shown in Fig. 13.27 has good tendency with the benchmark.

Present framework applied the implicit time scheme with immersed boundary method to achieves the high accuracy and efficiency simulation in the computational acoustic of pronouncing sibilant fricatives. By validating with the benchmarks, the results have qualitatively good agreement. Moreover, the combination of immersed

boundary method and high-performance computing reduces the computational resource drastically. It indicates that this framework is a promising tool for human phonation problem. About the future work, the investigation of how the shape effect the phonation will conduct for helping designing the denture.

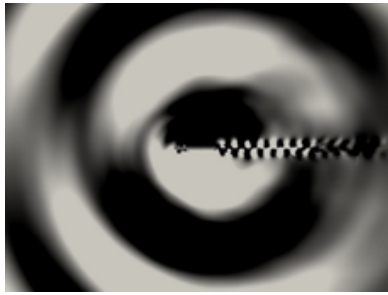


Figure 13.22: Contours of fluctuation pressure for phase- and spanwise-averaged flow fields.

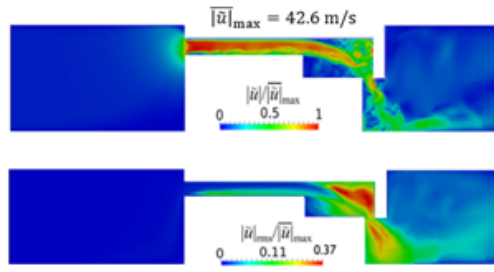


Figure 13.23: (Top) instantaneous and (bottom) RMS velocity magnitude.

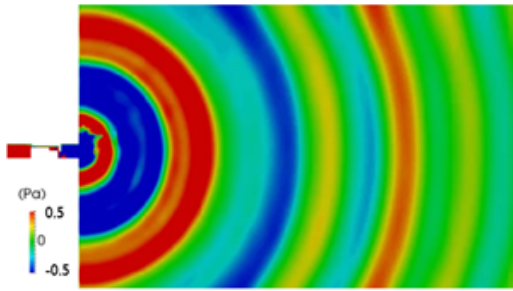


Figure 13.24: Fluctuation pressure of simplified model.

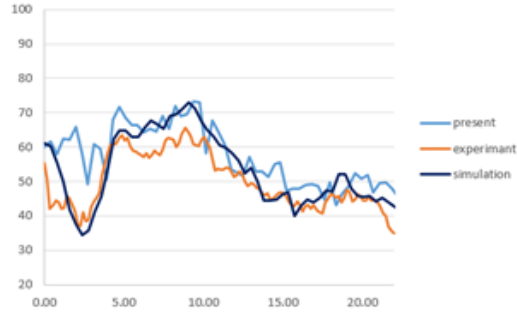


Figure 13.25: SPL spectrum of simplified model.

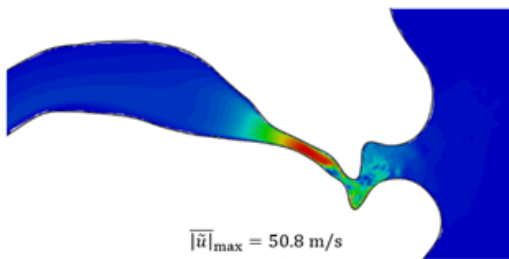


Figure 13.26: Instantaneous velocity magnitude of realistic model.



Figure 13.27: SPL spectrum of realistic model.

13.3.3.4 References

- [1] Yokoyama, H., K. Kitamiya, and A. Iida. *Physics of Fluids*, 25.10, (2013), 106104.
- [2] Nozaki K., Yoshinaga T., and Wada S., *J Dent Res*, 93(2), (2014), 207211.
- [3] Yoshinaga, Tsukasa, Kazunori Nozaki, and Shigeo Wada. *Physics of Fluids*, 30.3, (2018), 035104.

13.3.4 Speed-up and scale-up of fundamental methodology targeting post-K system

13.3.4.1 Performance optimization of incompressible solver of CUBE

This year, we evaluated and tuned the performance of the incompressible solver of CUBE on the K-computer. The target problem is a simple cavity flow, which targets a standard numerical scheme used for empirical analysis (Multigrid + CG method). The serial tuning of the relevant part was performed by cutting out the Poisson's equation solver by the multigrid method, which is the most costly part in the incompressible solver (accounting for 91% of the total). Specifically, the following measures were applied.

1. The integer operation for address calculation has been reduced by making the array referenced as a structure member directly referenced using a pointer.
2. Improved continuity of data access by swapping the dimensions of the array
3. The continuity of data access was improved by changing the array elements colored in red and black by Red-Black ordering so that they are stored in separate arrays.

As a result, a performance improvement of 9.8 times was obtained. Next, the following two tunings were applied as parallel tuning.

1. In the packing process for neighbor communication, the cost imbalance between threads has been improved by setting the division target of thread parallelization from each side of the subdomain to the cube (collection of cells) included in each side.
2. By changing the OpenMP thread scheduling scheme from dynamic to static for the computational loop included in the CG method, the cost balance between threads is improved and the overhead of dynamic scheduling is reduced.

As a result of these tunings (and the above-mentioned serial tuning), the performance of the entire program was improved by 2.9 times at 8,192 nodes in the K computer. As a result, it can be said that the speedup for creating results using "Fugaku" has been completed. However, there are still unknown parts about the evaluation of scaling when the number of nodes is further increased and the expected increase in collective communication cost, so we plan to deal with these in the result creation phase in the future.

13.3.4.2 Basic research for constructing a flow solution method using a neural network

In preparation for the coming era of computational science with AI initiatives, we are conducting basic research on prediction technology based on neural networks, which is expected to be used in the future in this research project. This year, we tried to reconstruct the flow field for the two-dimensional flow calculated by the unified solution code CUBE based on the neural network (CNN) using the convolutional filter as a machine learning technology that can be used at present. The following network is constructed by following the method [1] of replacing POD (Proper Orthogonal Decomposition) with a neural network for the flow field of the flow around a cylinder.

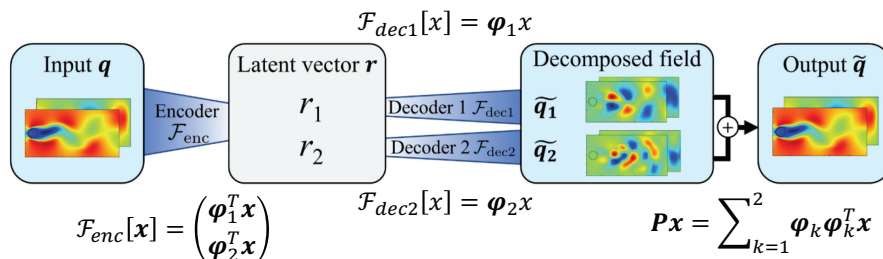


Figure 13.28: Structure of neural network (partially modified figure in paper [1]).

A neural network was trained for 10000 samples of snapshots as input, and the output was evaluated. As a result, the mode decomposition equivalent to that of reference [1], that is, the flow field was decomposed into two modes by a neural network, and the original flow field was reconstructed by synthesizing them, and the

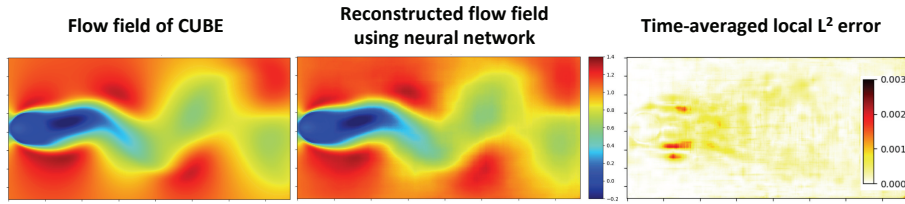


Figure 13.29: Example of flow field reconstruction results.

accuracy was equivalent to that of reference. It was confirmed that the flow field could be reconstructed. Figure 13.29 shows an example of the results.

Currently, only 2D is handled due to computational resources and technical restrictions, but we plan to expand this method in the future and evaluate the effectiveness of this method for 3D problems.

13.3.4.3 Unified solver extension using Adaptive Mesh Refinement (AMR)

Adaptive Mesh Refinement (AMR) has been found to be useful and effective for capturing fine structures in fluid analysis, such as where the gradient of a fluid state variable is steep, typically around a fluid-solid interface. Since the calculation grid is dynamically subdivided only where necessary for the solution and shape of the flow that changes quickly, it is not necessary to arrange a high-resolution calculation grid in the entire calculation domain. Costs are significantly reduced, especially in the unified multi-physics analysis such as the moving boundary problem. However, the calculation load balancing for high parallel computing is well known as a difficult task to implement.

The CUBE developed in this research project already has a hierarchical data structure, and has a solution for complex shapes, complex problems (heat, sound, chemical reaction, etc.) and moving boundaries. So, the best approach to introduce the AMR method is to build an extension of the solver. To examine the direction of the approach, we conducted a feasibility study based on several well-known open source softwares, including AMReX [2], which is being developed mainly by the Lawrence Berkeley National Laboratory in the United States. As a first step, we ran some basic simulations in search of new features suitable for our code. Figure 13.30 shows an example of the calculation applied to the vortex movement problem. It can be seen that as time progresses, the subdivided regions of the grid also move. Early studies provided important insights in investigating the low implementation effort and missing features in the available code. In the future, we plan to continue more detailed investigations and finally consider implementing it into CUBE.

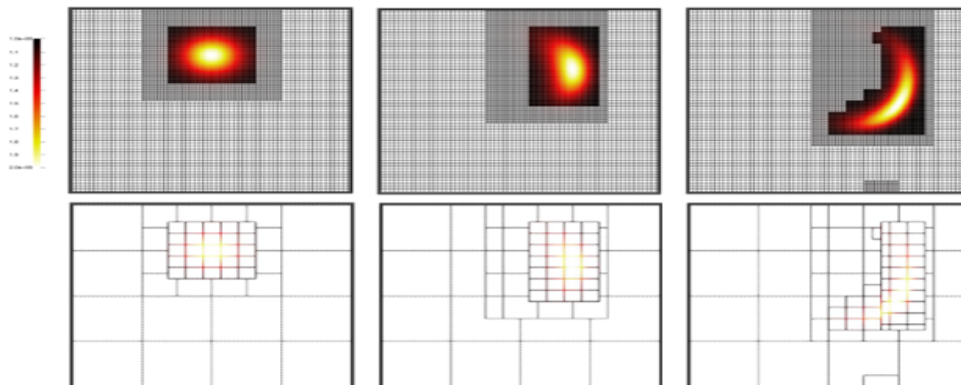


Figure 13.30: An adaptive mesh refinement solution for a typical advection problem.

13.3.4.4 References

- [1] T. Murata, K. Fukami, and K. Fukagata, “Nonlinear mode decomposition with convolutional neural networks for fluid dynamics,” *J. Fluid Mech.* 882, A13 ,2020.
 [2] AMReX-Codes, <https://amrex-codes.github.io/>, (cited 1st mar. 2020).

13.3.5 Strategic development and deployment of industrial software for the construction of digital engineering test beds

13.3.5.1 Realistic automotive engine cycle simulation for the evaluation of the mixing efficiency

As part of the development of an automobile engine testbed, we performed a fuel-air mixing analysis that assumed a practical usage scenario. The fuel-air mixing efficiency plays an important rule for automotive engine design. Generally, through the observation of the fluid structures of the tumble and the swirl shown in Figure 13.31, the efficiency can be evaluated.

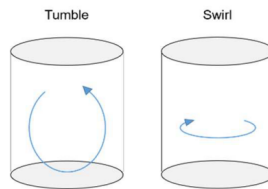


Figure 13.31: The tumble and the swirl.

However, this kind of the turbulent structure is not easy to obtain from the experience. Therefore, the aim of this study is to simulate the cold flow inside the engine using CUBE and visualize the turbulent structure to capture the tumble and swirl. Finally, the different shape of the piston is simulated to evaluate the performance to show that this framework is suitable for the industrial applications. The governing equation and numerical method of this study is as follows.

$$\frac{\partial U}{\partial t} + \frac{\partial F_1}{\partial x_1} + \frac{\partial F_2}{\partial x_2} + \frac{\partial F_3}{\partial x_3} = 0$$

The quantities included in U and F_i are

$$U = \begin{pmatrix} \rho \\ \rho u_1 \\ \rho u_2 \\ \rho u_3 \\ \rho e \end{pmatrix}, \quad F = \begin{pmatrix} \rho u_i \\ \rho u_i u_1 + P \delta_{i1} - \mu A_{i1} \\ \rho u_i u_2 + P \delta_{i2} - \mu A_{i2} \\ \rho u_i u_3 + P \delta_{i3} - \mu A_{i3} \\ \rho(e + P)u_i - \mu A_{ij}u_j - k \partial T / \partial x_i \end{pmatrix}$$

where $A_{ij} = \partial u_i / \partial x_j + \partial u_j / \partial x_i - 2/3(\nabla u \delta_{ij})$ and P is the pressure given by the ideal gas equation, $P = \rho RT$. The low-Mach-fix for Roe (LMRoe) scheme [1] with 5th order MSUCL reconstruction [2] is utilized in convection term and second order central difference is used for the viscous term. For the moving geometry, the immersed boundary method (IBM) which has been implemented in CUBE [3,4] is adopted to the engine motion including intake valve, exhaust valve and piston movement. First, the standard shape of the engine is simulated and the conservation is calculated to validate the practicality of the framework. The computational parameter and the physical model are shown in Figure 13.32. Three different time steps are adopted.

The comparison of the results with the theoretical values from ideal gas state equation is shown in Fig. 13.33. According to the result, when the $CFL < 10$, the distribution of the density, pressure and temperature has acceptable agreement with the theoretical result. The suggested reason for the discrepancy is that using the IBM causes the leakage.

Next, the comparison of the different shape of the piston has been conducted. The computational parameter and the different shape of the piston are shown in Figure 13.35. The visualization result of the streamline with the contour of the velocity magnitude is utilized to evaluate the magnitude of the tumble and swirl.

Tab.1 Engine parameters

Engine type	4Cycle Single Cylinder
Bore [mm]	90.0
Stroke [mm]	98.0
Conrod length [mm]	157.5
Piston offset [mm]	9.2
Compression ratio	10.4
Rotational frequency [rpm]	2000

Tab. 2 Initial conditions

Pressure at inlet boundary p_{in} [Pa]	97758.0
Pressure at outlet boundary p_{out} [Pa]	107605.5
Pressure in cylinder p_0 [Pa]	107605.5
Viscosity μ [Pa·s]	1.85×10^{-5}
Density ρ [Kg/m ³]	1.1842
Gass constant R [J/(K·kg)]	287
Specific heat ratio γ	1.4
Wall condition	Adiabatic

Tab.3 List of evaluated time steps

Time step Δt [s]	2.0×10^{-5}	1.0×10^{-5}	5.0×10^{-6}
Minimum cell size Δx [mm]	0.5	0.5	0.5
Courant number	14.28	7.14	3.57
Cube number	4,912	4,912	4,912
Cell number	20,119,552	20,119,552	20,119,552



Shape of engine



Shape of Piston

Figure 13.32: The simulation conditions of the standard shape.

Figure 13.36 shows the results of the visualization result of the streamline with the contour of the velocity magnitude. The result shows that with the convex at the left side of the piston in shape2, the velocity will be decreased. On the other hand, shape1 and 3 still keep strong tumble. However, at the left side of the engine, the tumble in shape3 becomes very weak. Overall speaking, shape1 obtain the strongest tumble.

Figure 13.37 shows the results at CA270 (Crank angle at 270 degrees). The result shows the same trend as Fig. 5 that shape1 is the best shape. However, with the convex shape, the swirl will be enhanced because the flow field will not be symmetric anymore. The flow field in shape3 is not only in vertical direction but also in horizontal direction so the swirl structure can be confirmed.

The results show that the current framework can be a useful tool for the engine design by giving a detail insight of the flow mechanism. However, the calculation condition is still under the cold flow condition. In next step, we are planning to model the combustion inside the engine and conduct direct evaluation of combustion energy efficiency. And also we have started to provide this framework to the industrial user for the evaluation of the usability of the framework. We will continue to improve practicality through the consortium activities.

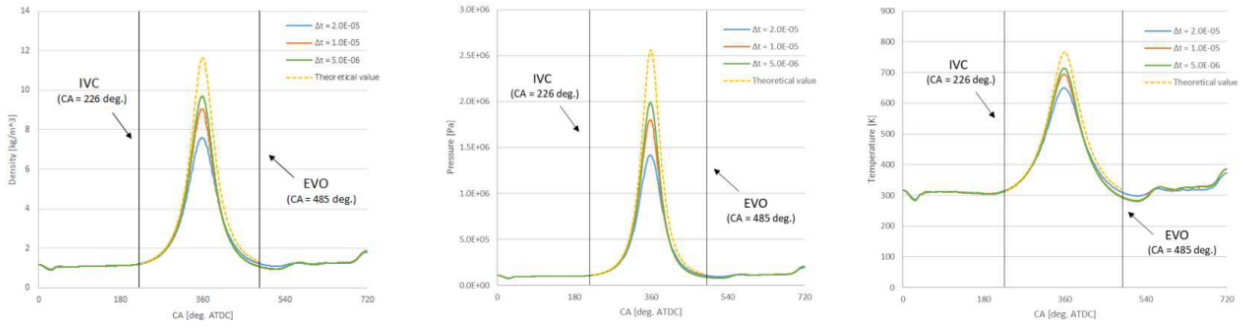


Figure 13.33: The comparison of the density, pressure and temperature.

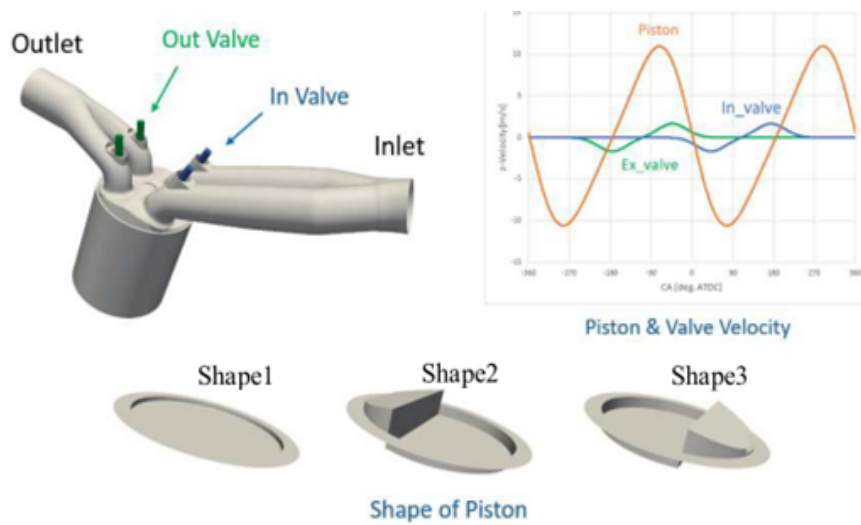


Figure 13.34: Engine cycle condition and piston shapes.

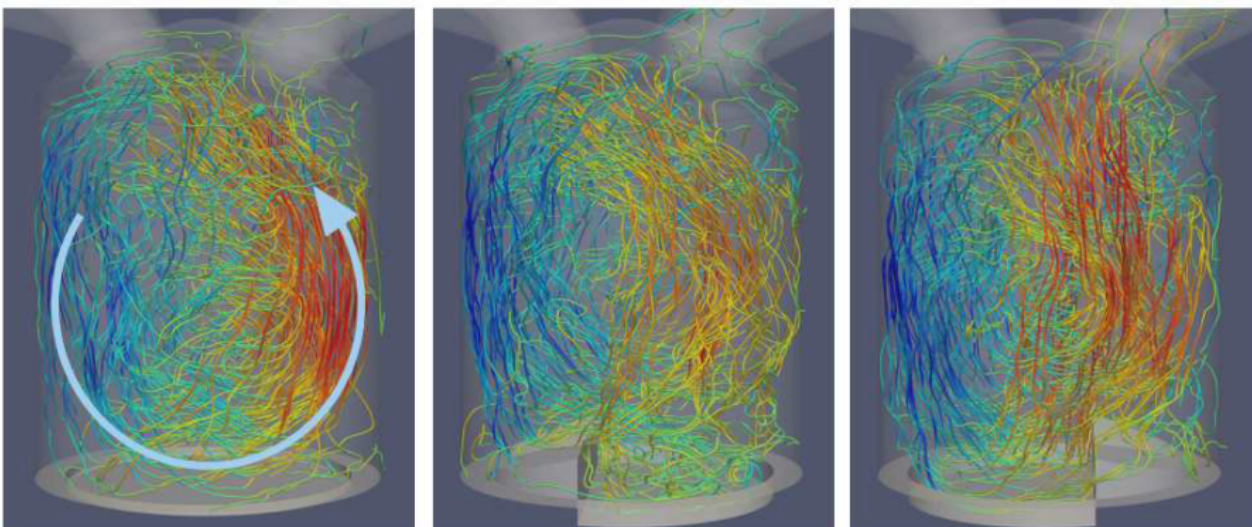


Figure 13.36: The streamline with the contour of the velocity magnitude at BDC.

Engine Type	4Cycle Single Cylinder		
Bore [mm]	78.0		
Stroke [mm]	83.6		
Conrod Length [mm]	133.0		
Piston Offset [mm]	0.5		
Rotational frequency [rpm]	2000		

	shape1	shape2	shape3
Time step Δt [s]	5.0×10^{-6}	5.0×10^{-6}	5.0×10^{-6}
Minimum cell size Δx [mm]	0.5	0.5	0.5
Courant number	3.57	3.57	3.57
Cube number	3,305	3,285	3,289
Cell number	13,537,280	13,455,360	13,471,744

Figure 13.35: Engine simulation conditions.

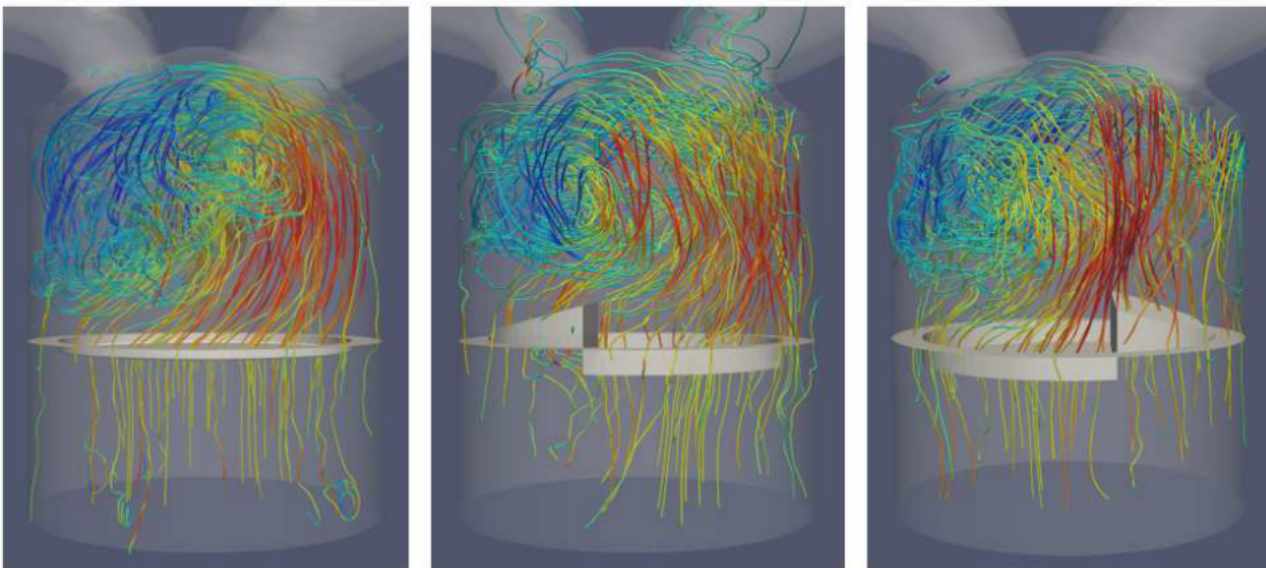


Figure 13.37: The streamline with the contour of the velocity magnitude at CA270.

13.3.5.2 Numerical simulation of flow in a fuel-injector of an aircraft engine

As a first step of the development of the combustion system test bed, the flow simulation of the jet engine combustor was performed. An investigation of grid sensitivity on local mesh refinement of numerical simulation of cold-flow in a fuel-injector of an aircraft engine was performed. In the case of an aircraft engine, a critical variable that governs emission, efficiency, and reliability is the equivalence ratio inside the combustion chamber. This value is transported by swirling turbulent flow from fuel-injector to the combustion chamber. Therefore, prior to precise prediction and appropriate control of the combustion characteristics of the engine, as a first step, the transport characteristics of flow through fuel-injector can be investigated through cold flow simulations. A complete evaluation of flow characteristics of the engine requires numerical simulation with the entire annular combustor geometry, which demands massive computational resources. Thus, an optimization strategy to minimize the computational cost through mesh optimization is warranted.

The cold flow simulations were carried out using CUBE, which is developed through this research. CUBE is a multiphysics simulation framework designed for large scale industrial simulations. A hierarchical meshing

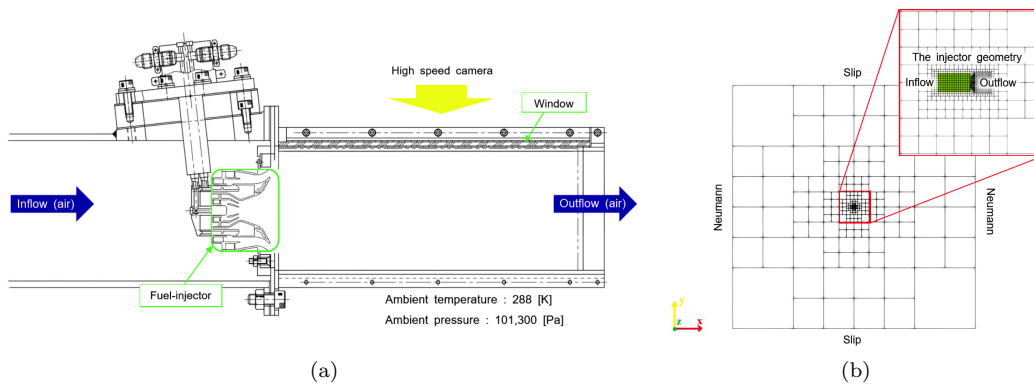


Figure 13.38: (a) The PIV measurement setup, (b) Numerical mesh and boundary condition

technique known as building cube method (BCM) is the foundation of CUBE over which numerical solvers are built. Even with the use of BCM for meshing the fuel-injector geometry, using a same near wall spacing mesh over the entire geometry results in excessively large numerical mesh. Consequently, relevant geometric components of the injector that strongly influence the flow have to be identified for mesh refinement while coarser mesh can be used for rest of the geometry. Then it is important to investigate the dependence of flow on the refined mesh and to minimize the total mesh size while ensuring accuracy. The governing equations used in this study are same as previous section. This is fully compressible flow approach. A 2D PIV measurement of air flow in a fuel-injector was conducted by Kawasaki Heavy Industries. The detail flow field results were compared with the measurement result. The experimental setup and the measurement window are shown in Fig. 13.38. In order to validate the accuracy, a very high-resolution mesh was used. The geometry used in the simulation is highlighted as the fuel injector in Fig. 13.38. The boundary conditions and the mesh are also shown in Fig. 13.38. The wall boundary condition, which means the boundary condition on the surface of geometry, was set as adiabatic condition. The inflow mass flow rate was set as the same value of PIV measurement and the ambient pressure 101,300 Pa, ambient temperature 288 K was set. The finest mesh resolution was 0.05 mm and the number of calculation mesh was 500 million. The 2048 nodes of K-computer was used and the calculation time was 48 hours to obtain the physical solution time of 2.7 s.

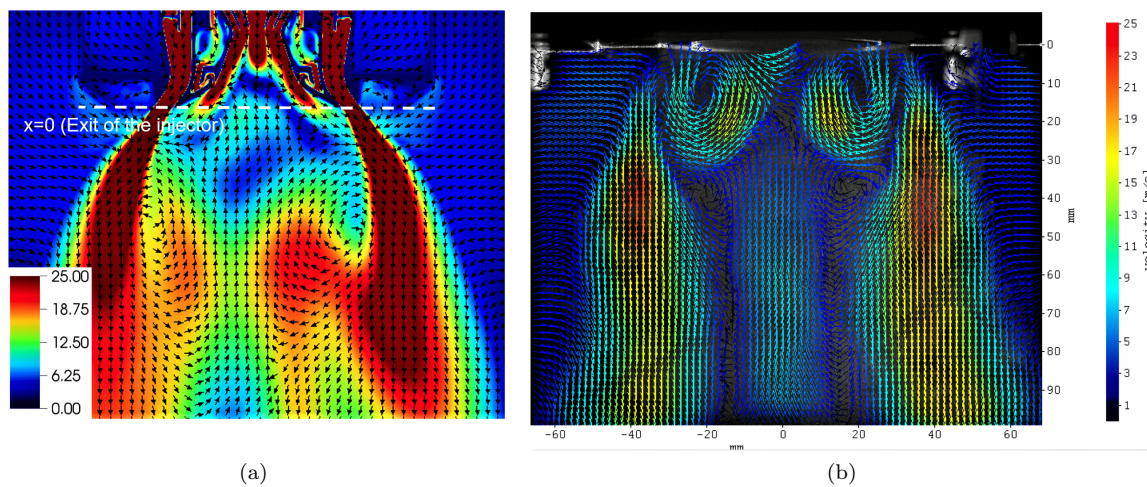


Figure 13.39: (a) Time averaged velocity magnitude high-resolution simulation, (b) Time averaged velocity magnitude 2D PIV data

Velocity magnitude contours on a mid-sectional plane from the PIV measurement and the numerical simulation are shown in Fig. 13.39. Four distinct identifiable flow signatures, in the exit plane are identified in

Fig. 13.40. The flow signatures are termed as A, B, C and D, in the PIV result, and A', B', C' and D' in the simulation result. First, A (and A') is the primary jet emanating out of the injector. A' shows greater velocity magnitude than A. In both cases, the flow gradually decelerates as it heads downstream. The flow signature B is formed by the flows from the pilot region and air-silt nozzle. It is observed that B is separated from A and forms vortex. On the other hand, B' does not form any vortex but just joins into A', supplying momentum to A'. It is hypothesized that intrinsically, B' is just sucked into A' because of the large velocity magnitude in the exit-vicinity region of A'. Meanwhile, C' is more widely distributed although C is localized in narrow region. It is regarded that the absence of vortex in B and the intensity difference primary jet (A-A') may affect the distribution. Furthermore, the velocity magnitude of the flow in C' greater than the flow in C and it is likely that this is due to the difference in intensity of the primary jet, i.e. A-A', which induces C-C'. Finally, D' stretches longer than D up to the exit of the injector. It can be considered that the greater intensity in the region C' and the absence of vortex in B' assists the flow in D' stretching it longer than its PIV counterpart D.

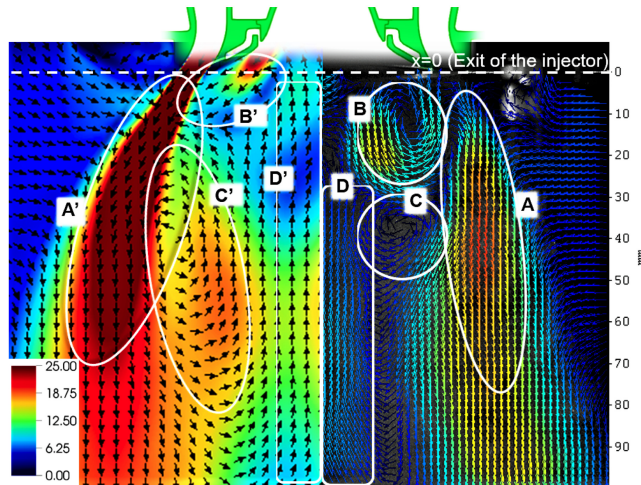


Figure 13.40: A comparison of the simulation and PIV results: 4 prominent features can be identified in each case.

To sum up, the overall difference of the velocity magnitude is due to that PIV data does not contain the depth component. Meanwhile, it is regarded that the local differences are mainly affected by the difference between B and B' induced by overestimation of A'. Therefore, this is the sole qualitative difference between the simulation and the PIV data. It can be inferred that the simulation qualitatively resolves the injector flow. In the next step, we are planning to develop the fuel spraying model and the combustion model which is specifically designed for the real engine combustors. We will continue to develop the functionality to reproduce the real state of engine combustion through the consortium activities.

13.3.5.3 Construction of surrogate model by aerodynamic multipurpose shape optimization analysis and machine learning

In this study, we have developed a multipurpose optimization analysis framework using CUBE for the purpose of efficiently optimizing aerodynamic performance at the initial design stages. This framework provides CHEETAH [5], a multipurpose evolution optimization software, in collaboration with the Japan Aerospace Exploration Agency. CUBE has a data structure with a hierarchical Cartesian grid, and MeshWorks [6] is applied, which is a shape morphing software by Detroit Engineered Products, Inc. It is a method that can be shared with a single calculation grid for a plurality of changing vehicle shapes, and can avoid problems related to calculation grid generation and morphing.

Continuing from last year, we performed genetic-evolutionary computation up to the 12th generation with a 4-objective function with the aim of obtaining an index of robustness against changes in the wind direction of sedan-type automobile models. The population size was 18, and a total of 252 cases of $36 + 18 + 18 \times 12$ generations including individuals in the L36 orthogonal table for generating the initial generation population. And 2 wind directions for each needed to be calculated. Each case was calculated with 367 nodes of “K-computer” with 14 hours, and the total amount of calculation was about 2.6 million node-hours (including the

amount used last year). Figure 13.41 shows the Pareto solution for the difference between the aerodynamic resistance value (C_d) and the resistance to the wind direction (ΔC_d). The tendency of the objective function value similar to the knowledge obtained in the actual design was reproduced, and the validity of the framework could be confirmed.

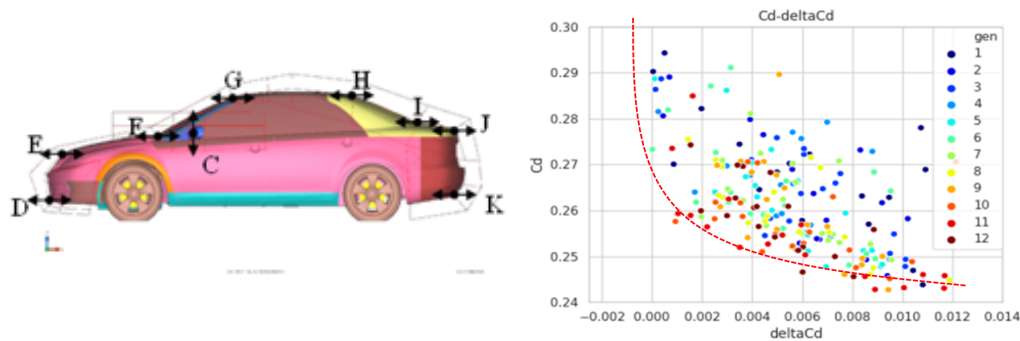


Figure 13.41: The geometry deformation parameters (left) and optimized results of Pareto solution on 12th generation (right).

In this physical year, we tried to build a surrogate model by machine learning utilizing these results as training-data. For neural networks constructed using Sony’s Neural Network Console [7], 18 individuals \times 1 to 6 generations = 108 models were used for training-data, and 18 individuals \times 7 to 12 generations = 108 models were used for evaluation-data. The input was 9 design variables, and C_d and ΔC_d were targets. Figure 13.42 shows the aerodynamic drag obtained by calculation and the predicted result by machine learning. The C_d value was predicted almost accurately, and it could be confirmed that the constructed neural network was appropriate. It has also been confirmed that the Pareto solution based on this prediction result shows the same tendency as the solution obtained by the actual CFD calculation. This suggests that machine learning can be a powerful design tool in the future if appropriate design variables can be selected. However, there are some models whose prediction results are different with respect to the difference in aerodynamic drag, and there are also subtle differences in the obtained sedan-type optimum body shape. We are proceeding with consideration including investigation of the factors causing it. In the future, we plan to introduce design variables that reproduce more detailed shapes and improve the degree of freedom, which will lead to the creation of results in “Fugaku”.

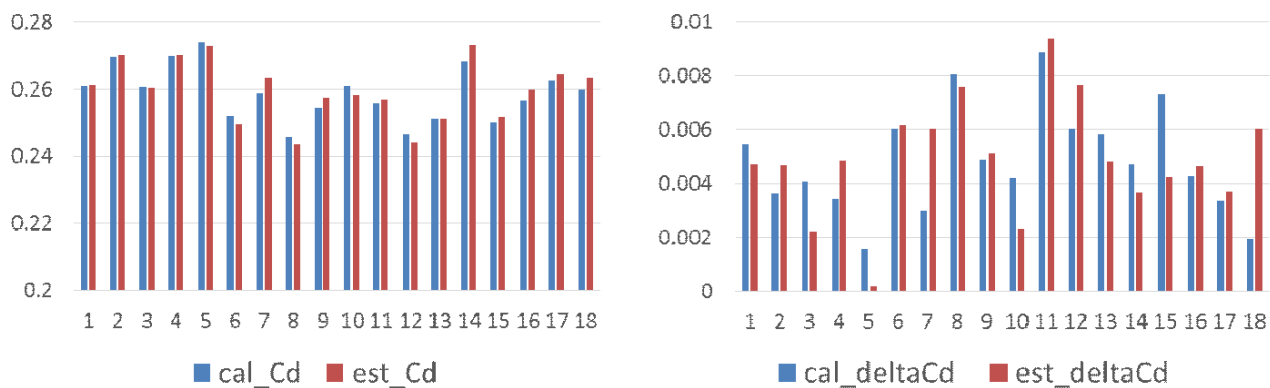


Figure 13.42: The prediction results using machine learning (left) drag (right) drag difference between 0 and -3 yawing angle.

13.3.5.4 Wind resistant design of building structures – fluid structure coupled analysis of high-rise towers

As an issue of the architectural consortium, verification analysis of a test bed based on a unique fluid structure coupled analysis method was performed. In recent years, with the increase in the height of buildings and the reduction in the weight of construction materials, there have been increasing cases of construction of high-rise buildings and large-scale structures having roofs using light materials. Since the design of these structures requires low attenuation due to weight reduction, it is necessary to examine the wind resistance as well as the seismic resistance for earthquake. In particular, unstable aerodynamic vibrations caused by the interaction between the vibrations of the building itself and the flow field around the building due to the turbulence of the wind have a risk of causing a large amplitude leading to collapse of the building. Generally, a building is heavy and hard to be deformed as compared with a bridge or other structure. Therefore, conventionally, there has been no problem with dynamic vibration, and it has been a problem to secure the building resistance to a static wind load. However, with the emergence of such high-rise buildings, it has become important to study the problem of vibration when the buildings are subject to strong winds. Thus, it is important to grasp the structural characteristics in wind load evaluation. Figure 9 shows the mechanism of the generation of unstable vibration generated by the interaction between wind turbulence and the vibration of the building itself. Vigorous research has been conducted on the unstable vibration phenomenon of buildings in the past, however there are still many unknowns about the mechanism of occurrence and the influence of the interaction between them, and aerodynamic instability. It has been pointed out that when studying unstable phenomena such as vibration, the phenomena cannot be reproduced unless the structure and the surrounding flow field are treated as a strongly coupled problem. There is few software that can achieve this. In this project, we have developed a unique fluid-structure strong coupled unified solution that combines marker particles with the Euler-type structural analysis method. In order to prove the validity of the method, detailed verification analysis was performed using basic tower structure.

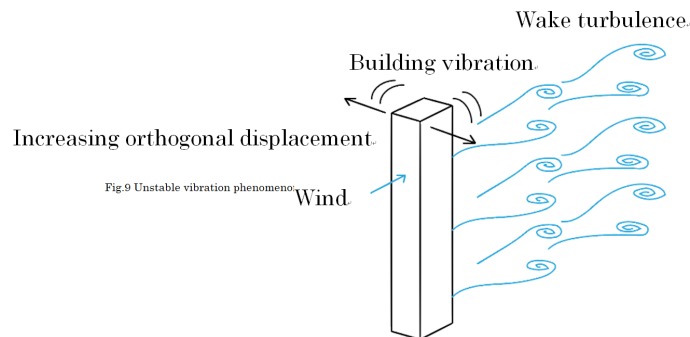


Figure 13.43: Unstable vibration phenomenon of high-rise building.

In order to verify the validity of this method, first, a fluid-structure interaction analysis with a rigid structure was performed. The structural shape is a quadrangular prism of $0.1 \times 0.1 \times 0.1m$. We compare it with the results of previous experiments. The calculation conditions, analysis mesh and inflow fluctuation wind are as follows.

Figure 13.48 shows a comparison with the results of previous wind tunnel experiments. The black line represents the result of the calculation by this method, and the blue line represents the result of the previous experiment, and it can be confirmed that the values agreed well.

Considering the introduction of this method to architectural structures, numerical stability was examined by performing analysis with various conditions of prismatic structures. Four cases were prepared in which the Reynolds number was fixed at 10, the mass density difference between the solid and the fluid, and the shear modulus of the solid has been changed. The analysis results are shown in Fig. 13.49-13.50. From these results, it was found that numerical instability occurred near the prisms in all models due to the numerical calculation method of solid strain. In the next step, we plan to introduce a method that can stably calculate the solid strain without depending on the velocity field. We will continue to develop the functionality to produce the practically useful framework for the strong-coupling fluid-structure interaction through the consortium activities.

Calculation region	X : -0.55~1.45, Y : -0.5~0.5, Z : 0~2.0 (m)
Mesh	About 36000000
Minimum cell size	0.000577(m)
Re	55846
Resolution	$\Delta t = 0.0005, 0.0050(\text{Minimum})$
Timeintegration	2nd order Crank-Nicolson
Spatial discretization	Convective term : 2nd order Central + 5% Upwind Diffusion term : 2nd order Central
Boundary condition	Inlet : Inflow turbulence Outflow : Convective Wall : Volume Constraint IBM, Side, Top : Slip
Iteration number	30
Pressure convergence	1d-5

Figure 13.44: Calculation conditions.

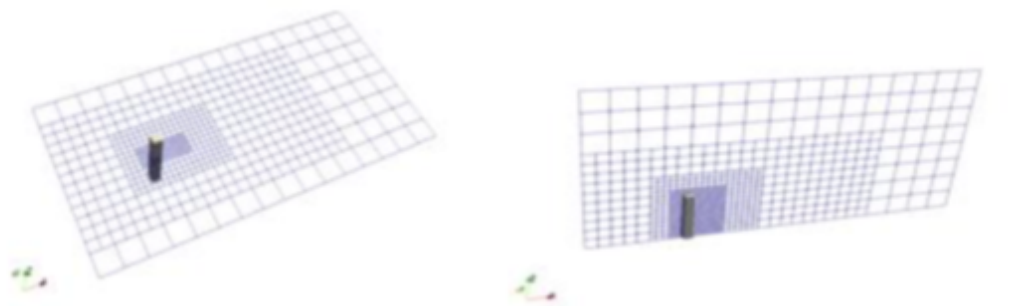


Figure 13.45: CUBE mesh.

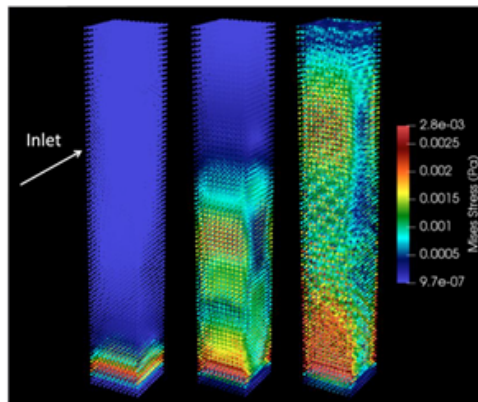


Figure 13.49: Mises stress distribution of bility of each case. CASE-D.

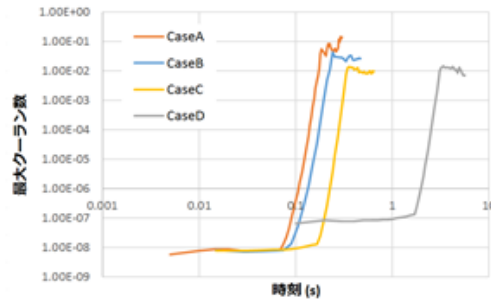


Figure 13.50: Comparison of calculation sta-

Finally in this fiscal year, we conducted a simulation of wind resistance analysis of the dome roof of a stadium structure as an application to practical problems. The flow condition is 10 m/s of air wind, the Reynolds number is approximately 273 million, and the soft material property is set as 33,300 Pa of elastic modulus, $300kg/m^3$ of the mass density of solid. The number of the cell was approximately 17 million, and the calculation time was 10 hours using 256 nodes of K-computer. Figure 13.51 shows a typical flow field coupled with the soft material deformation of the stadium roof. We cannot say anything about the validity of this result or its physics yet. However, this result may be the world's first example of solving FSI problems at a high Reynolds number over hundred million by an Eulerian FSI method. At least, we did not observe the unphysical deformation of the roof region (sponge) induced by wind force. In the next step, we plan to increase the resolution of calculation mesh to try to capture smaller flow structures and deformation modes. We will continue to contribute to help users to apply this method into the practical cases through the consortium activities.

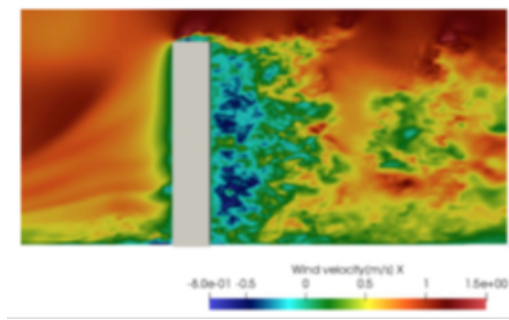
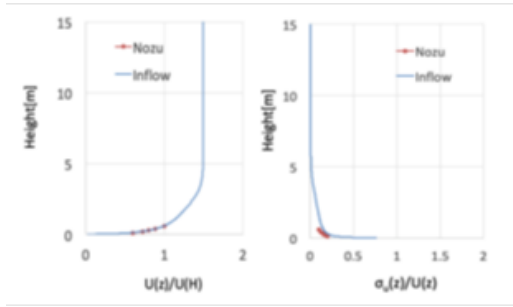


Figure 13.46: Inflow fluctuating wind profile. Figure 13.47: X-direction velocity distribution in vertical section of prism.

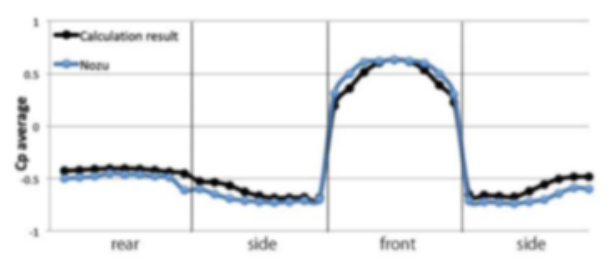


Figure 13.48: Horizontal mean wind pressure coefficient distribution of prism: comparison with previous experimental results.

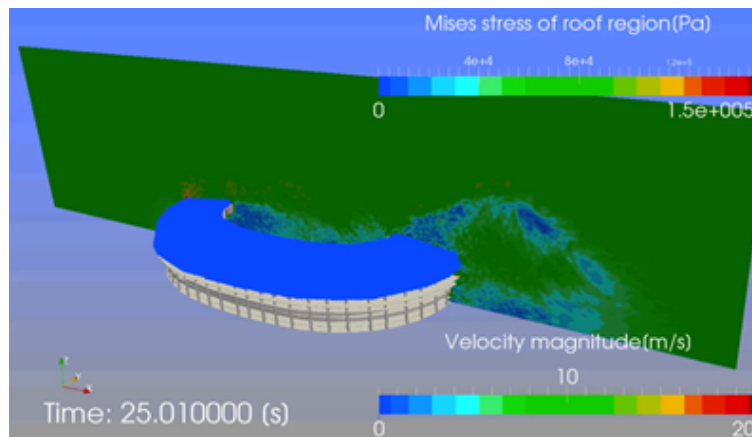


Figure 13.51: Example of flow and stress results on deformable roof analysis for a stadium structure.

13.3.5.5 Topology optimization using Eulerian structure analysis

Topology optimization [8] is a method to determine the arrangement of materials and components, including the voids, to maximize or minimize the objective function using a limited material volume in the design space. In recent years, industrial applications of topology optimization have been increasing as it provides effective suggestions to designers. On the other hand, when considering the application to a real product, the volume of the actual product material is usually less than 1% of the design area expected by the designer. In addition to this, the preparation of design-domain shape modeling, which includes many cases and trials in the upstream of the design process, requires a lot of time and effort. In this study, we are developing an original unified fluid-structure analysis method based on Eulerian methods combined with the Lagrangian marker particle method to solve a large-scale structural analysis problem which is difficult to be solved by conventional methods. The

marker particle method is one of the most promising methods to solve the topology optimization challenges mentioned above, because it is easy to achieve high parallelization efficiency and to reduce the time and effort of mesh generation in a massively parallel computing environment. In this year, we have developed a topology optimization framework using Eulerian structural analysis method. To verify the validity of the topology optimization, the optimization of the maximum amount of energy absorbed by a two-dimensional structure with a circular hole in the center of the design region under enforced velocity loading in the direction of shear was carried out. The results are comparable to those obtained by the finite element method, even when CUBE is used. In addition, the quantitative value of the objective function also approaches that of FEM by increasing the spatial resolution.

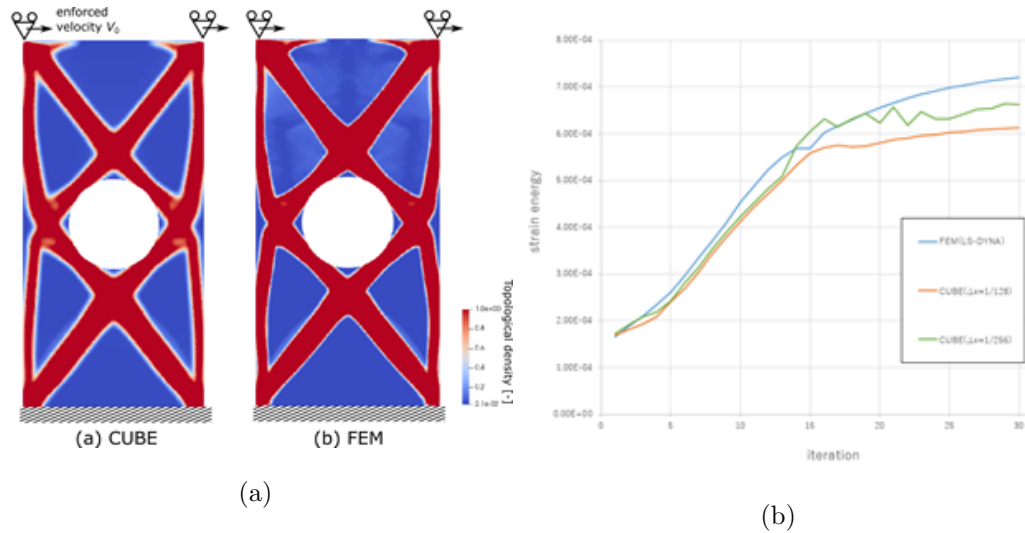


Figure 13.52: Optimal shape as a result of topology optimization to maximize absorption energy by shear enforced velocity load (left), and its objective function history (right).

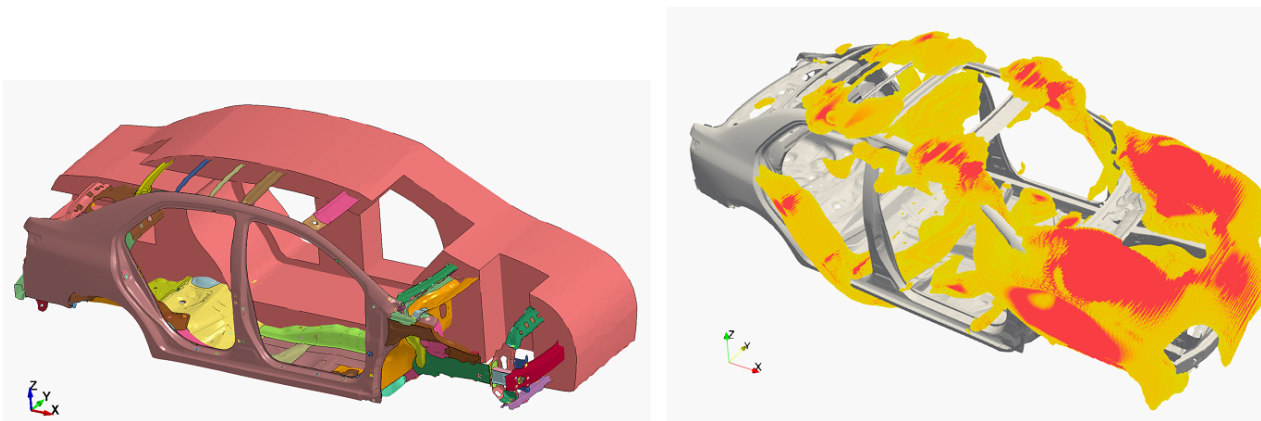


Figure 13.53: Design area which surrounds a conventional white body frame (left) and optimal shape as a result of topology optimization subject to torsional enforced velocity load (right).

Using this framework, we performed optimization trials for a car body frame with 10 million design variables, which is somewhat difficult to do with existing topology software (Fig. 2). A design domain was set up over the white body frame of an existing published body model (TOYOTA, Yaris 2010, [9]), and forced-velocity loads were applied to the design domain to maximize the amount of energy absorbed by the body torsion. As a result, a frame structure close to the intended white body frame was obtained. In the future, we will continue to carry out various basic verification examples and optimization verifications for a large number of load cases that are

assumed to be real problems, as well as to improve the optimization performance through collaboration with industry.

13.3.5.6 Implementation of aerodynamic body motion coupled analysis framework

In recent years, it has become clear that the evaluation of unsteady aerodynamic force that reproduced in the actual running state is indispensable for the aerodynamics parts design, since it affects the evaluation of steering stability of automobiles. In general, it is difficult to accurately capture the flow field around a vehicle during actual driving motion and to measure changes in vehicle attitude. And the actual driving test is affected by atmospheric disturbances, so the same situation should be reproduced. Additionally, it is difficult to evaluate the steering stability by quantitative evaluation depending on the driver's experience. Therefore, in this research, we constructed an analysis framework that can reproduce the actual driving state by combining aerodynamic analysis with vehicle motion on a supercomputer, which includes suspension, steering mechanism and driver's operation reaction, etc.

This framework adopts the implementation of the open source multibody dynamics analysis software, named Project Chrono [10], into the CUBE. It is possible to use commercial vehicle motion analysis software, but in order to operate it on a supercomputer, we have experienced problems such as binary support, license handling, and external communication of calculation nodes. So an open source framework is powerful solution, the significance of being able to do it is high rather than other researchers think. In this year, we succeeded in constructing this framework and implemented a practical example of vehicle motion analysis.

A hatchback type real vehicle shape model was used for the analysis. The model also reproduces detailed shapes such as underfloor and auxiliary equipment inside the engine room. We are comparing steering stability with and without aero parts mounted on the side of the vehicle. In this case, the suspension and steering mechanism of the same type as the actual vehicle could be used. Assuming a lane change movement to the overtaking lane-change maneuvering on the highway, the steering stability was evaluated for the movement to the right side 3 m at 100 km/h.

Figure 13.54 shows an example of visualization results of flow field and motion analysis. A correlation has been shown between the sensory evaluation of steering stability and the roll motion of the vehicle. When evaluated by focusing on the roll motion and the steering input by the driver (Fig. 13.55), both the angular velocity and the angular jerk (time change of acceleration) showed a decrease in peak and amplitude when the roll motion in the first half converged. Results consistent with the report were obtained in the driver's sensory test. In the future, we plan to make improvements to create results on "Fugaku" while conducting higher resolution analysis and improving versatility.

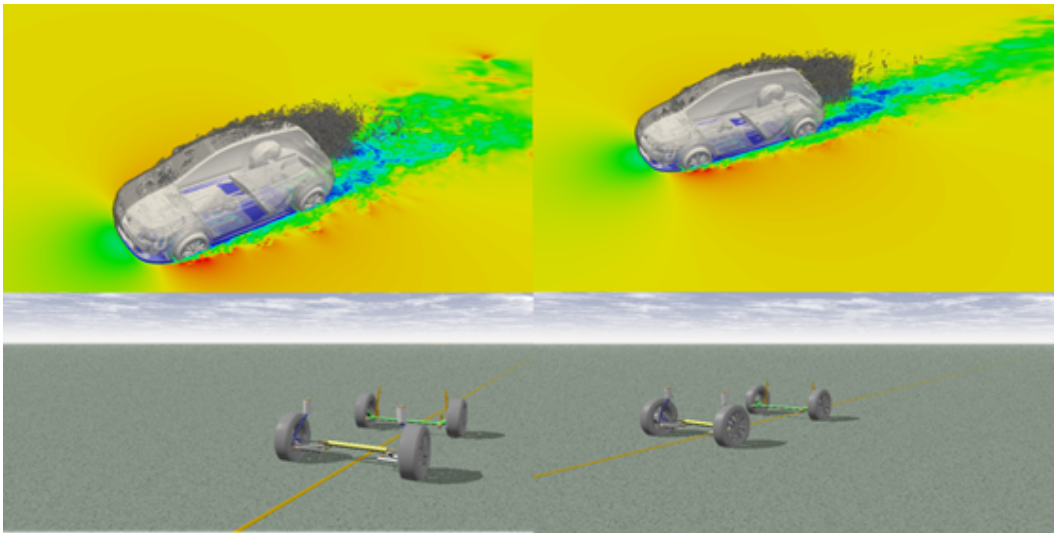


Figure 13.54: Analysis example of lane change maneuver (upper: CUBE result, lower: motion analysis visualization result).

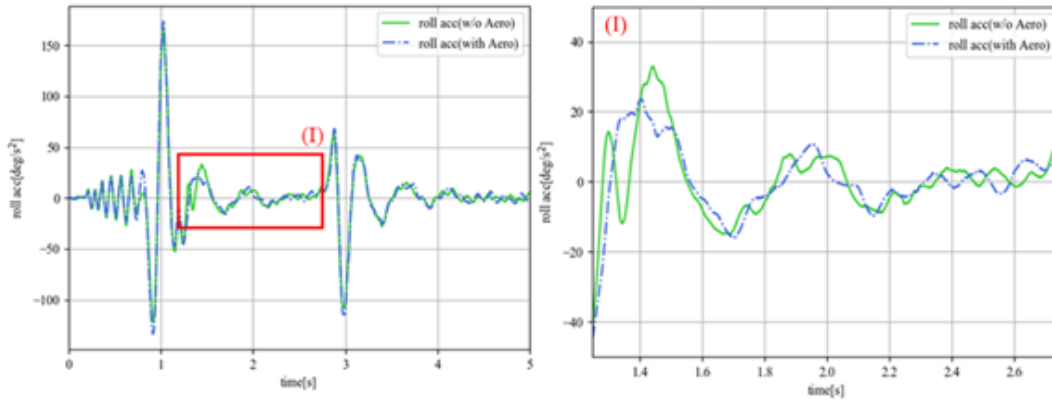


Figure 13.55: Results of roll angular velocity of vehicle motion.

13.3.5.7 References

- [1] F. Rieper, “A low-Mach number fix for Roe’s approximate Riemann solver,” *J. Comput. Phys.*, 230, pp. 52635287, (2011).
- [2] K.H. Kim, C. Kim, “Accurate, efficient and monotonic numerical methods for multi-dimensional compressible flows Part II: Multi-dimensional limiting process,” *J. Comput. Phys.*, 208, pp.570615, (2005).
- [3] C.-G. Li, M. Tsubokura, R. Bale, “Framework for simulation of natural convection in practical applications,” *Int. Commun. Heat Mass Transf.*, 75, pp.5258, (2016).
- [4] N. Jansson, R. Bale, K. Onishi and M. Tsubokura, CUBE, “A scalable framework for large-scale industrial simulations, International,” *Journal of High Performance Computing Applications*, Vol.33, pp.678-698, (2018).
- [5] A. L. Jaimes, A. Oyama, and K. Fujii, “A ranking method based on two preference criteria: Chebyshev function and e-indicator,” *Proceedings of 2015 IEEE Congress on Evolutionary Computation*, (2015).
- [6] MeshWorks WEB site, <https://www.depusa.com/meshworks/>, [cited 1 Mar 2020].
- [7] Neural Network Console WEB site, <https://dl.sony.com/ja/>, [cited 1 Mar 2020].
- [8] M.P. Bendsøe, N. Kikuchi: “Generating optimal topologies in structural design using a homogenization method,” *Comput.Methods in Appl.Mech.Eng.* Vol 71, No. 2, pp. 197 224 (1998).
- [9] Center for Collision Safety and Analysis: “2010 Toyota Yaris Coarse Finite Element Model Version 11”, 2016 Dec. URL: <https://www.ccsa.gmu.edu/models/2010-toyota-yaris/>
- [10] Project Chrono WEB site, <https://projectchrono.org/>, [cited 1 Mar 2020].

13.4 Schedule and Future Plan

In the research and development of unified simulation framework ‘CUBE’ from 2012, the following goals has been achieved:

1. Construction and development of the simulation technology for bringing out the performance of K-computer
2. Validation and practical usage of industrial applications such as vehicle aerodynamics, aeroacoustics, unsteady motion aerodynamics, engine combustion, city area wind environment analysys, sport CFD, and structure analysis
3. Preparation of the simulation technologies of HPC toward EXA-scale

In the long-term objectives, the following target is considered:

1. Establishment of the research and development center for industrial simulation technology
2. Contribution to computer science by expanding the developed simulation technology to different fields

In terms of using Cartesian grids, the problems that the analysis accuracy in the vicinity of the wall surface decreases due to the limitation of immersed boundary method is becoming clear. In the future, through the

deployment of CUBE to the industrial applications, the introduction of higher order schemes, wall modeling and advance sophisticated research of immersed boundary method are planning.

In terms of structure analysis, to avoid this numerical oscillation even when the spatial resolution is low, we are going to introduce a calculation method for solid deformation tensors that does not require velocity gradient calculation and we continue to work on development to improve analysis accuracy.

In terms of using Hierarchical grid system, the problems that the interface communication in each halo of cubes will spoil the performance on future supercomputers is becoming clear. In the future, the enhancement to the current communication / calculation overwrapping technique, or tuning for the interface communication, introduction of adaptive refinement scheme are planning.

From collaborative companies, including companies through the activities of the “Consortium for Next Generation Automotive CAE using HPC” and “Consortium for Next Generation Combustion CAE using HPC” organized by RIKEN, voices of surprises and expectation for software development have been received. We are planning to continue development for practical application in near future.

13.5 Publications

13.5.1 Articles/Journal

- [1] Rahul Bale, Neelesh A. Patankar, Niclas Jansson, Keiji Onishi, and Makoto Tsubokura, “Stencil Penalty approach based constraint immersed boundary method,” *Computers & Fluids*, Vol.200(30), 104457, (2020).
- [2] Koji Nishiguchi, Tokimasa Shimada, Masafumi Otaka, Shigenobu Okazawa, Makoto Tsubokura, “Eulerian finite volume formulation using Lagrangian marker particles for compressible solid analysis,” *Journal of Japan Society of Civil Engineers, Ser. A2 (Applied Mechanics (AM))*, 75(2), I-237-I-248, (2019).
- [3] Keiji Onishi, Makoto Tsubokura, “Topology-free immersed boundary method for incompressible turbulence flows: An aerodynamic simulation for ‘dirty’ CAD geometry”, arXiv preprint, arXiv:2002.06206, (2020)

13.5.2 Conference Papers

- [4] Keiji Onishi, Rahul Bale, Makoto Tsubokura, “Assessment of Rotating Wheel Vehicle Aerodynamics Simulation using Cartesian Grid Method and Open-grill Full Vehicle Models,” *SAE Technical Paper 2019-01-0660*, (2019).
- [5] Onishi Keiji, Jansson Niclas, Tsubokura Makoto, “In-situ visualization on large scale vehicle aerodynamics simulation,” In: *Proceedings of the 24th Conference on Computational Engineering and Science*, A-05, (2019).
- [6] Rahul Bale, Kazuto Ando, Yuki Hayashi, Keiji Onishi, and Makoto Tsubokura, “Analysis of underwater undulatory swimming using self-propulsion simulations,” In: *Proceedings of the 24th Conference on Computational Engineering and Science*, (2019).
- [7] Koji Nishiguchi, Tokimasa Shimada, Masafumi Otaka, Shigenobu Okazawa, Makoto Tsubokura, “Eulerian finite volume formulation using particle-in-cell method for large-scale parallel simulation of complex structures,” *Proceedings of ECCOMAS MSF 2019 THEMATIC CONFERENCE*, 4 pages, Sarajevo(Bosnia-Herzegovina), (2019).
- [8] Koji Nishiguchi, Rahul Bale, Tokimasa Shimada, Masafumi Otaka, Hirofumi Sugiyama, Shigenobu Okazawa, Makoto Tsubokura, “Eulerian finite volume formulation using Lagrangian marker particles for compressible solid analysis,” In: *Proceedings of the 22nd JSCE Applied Mechanics Symposium*, C000134, (2019).
- [9] Koji Nishiguchi, Tokimasa Shimada, Masafumi Otaka, Shigenobu Okazawa, Makoto Tsubokura, “Structure analysis with particle-in-cell method using hierarchical Cartesian mesh,” In: *Proceedings of the Conference on Computational Engineering and Science 24*, A-05-02, (2019).
- [10] Tokimasa Shimada, Koji Nishiguchi, Shigenobu Okazawa, Makoto Tsubokura, “Eulerian Unified Formulation Using Lagrangian Marker Particles for Fluid-Structure Interaction Problems,” In: *Proceedings of the 33th Computational Fluid Dynamics Symposium*, E11-4, (2019).
- [11] Hiromasa Kajimoto, Shunpei Koyama, Rahul Bale, Keizo Yamamoto, and Makoto Tsubokura, “Aerodynamics simulation framework for Ski-jumping take-off and its application to various jumpers,” In: *Proceedings of the 33th Computational Fluid Dynamics Symposium*, D01-4, (2019).
- [12] Yotaro Nomoto, Rahul Bale, Keiji Onishi and Makoto Tsubokura, “Construction of a Car Aerodynamic-Motion Coupled Analysis Framework Using Hierarchical Orthogonal Grid,” In: *Proceedings of the 33th Computational Fluid Dynamics Symposium*, B07-1, (2019).
- [13] Younghwa Cho, Rahul Bale, Chung-Gang Li, Tomonari Satoh, Ryusuke Matsuyama, Takeo Oda, Makoto

Tsubokura, Nobuyuki Oshima, “Numerical simulation of flow in a fuel-injector of an aircraft engine,” In: Proceedings of the 33th Computational Fluid Dynamics Symposium, (2019).

[14] Tetsuro TAMURA, Yong CAO, Yuki NAGAO, Hidenori KAWAI, Koji NISHIGUCHI, Makoto Tsubokura, “High performance computing of wind-induced pressures on various domes under real conditions,” Proceedings of the IASS Annual Symposium 2019 (FORM and FORCE 2019, Barcelona, Spain), pp.1185-1192, (2019).

13.5.3 Posters

[15] Kazuto Ando, Rahul Bale, Keiji Onishi, Kiyoshi Kumahata, Kazuo Minami, Makoto Tsubokura, “Optimizing Multigrid Poisson Solver of Cartesian CFD code,” SC19 - International Conference for High Performance Computing, Networking, Storage and Analysis, Denver(CO), (2019).

[16] Onishi Keiji, Bale Rahule, Tsubokura Makoto, “Research and development of automotive aerodynamic simulation method for WLTP,” Japan Society of Mechanical Engineers, the 97th Fluid Engineering Division Conference, (2019).

[17] Bale Rahul, Wang Wei-Hsiang, Li Chung Gang, Onishi Keiji, Uchida Kenji, Hidefumi Fujimoto, Tsubokura Makoto, “Numerical Simulation of Combustion in a Rapid Compression Machine (RCM),” Japan Society of Mechanical Engineers, the 97th Fluid Engineering Division Conference, (2019).

[18] Ando Yasunori, Li Chung Gang, Onishi Keiji, Tsubokura Makoto, “The Prediction of Narrowband Noise Emitted from Real Vehicle Shape,” Japan Society of Mechanical Engineers, the 97th Fluid Engineering Division Conference, (2019).

13.5.4 Invited Talks

13.5.5 Oral Talks

[19] Keiji Onishi, Yasunori Ando, Kosuke Nakasato, Makoto Tsubokura, “Assessment of Rotating Wheel Vehicle Aerodynamics Simulation using Cartesian Grid Method and Open-grill Full Vehicle Models,” WCX19: SAE World Congress Experience, Detroit (MI), (2019).

[20] Keiji Onishi, Makoto Tsubokura, “Toward Realization of Real-Time Vehicle Aerodynamics Simulation,” ASME-JSME-KSME Joint Fluids Engineering Conference (AJK Fluids2019), San Francisco, CA, (2019).

[21] Koji Nishiguchi, Rahul Bale, Tokimasa Shimada, Masafumi Otaka, Shigenobu Okazawa and Makoto Tsubokura, “Eulerian Finite Volume Formulation using Lagrangian Marker Particles for Deformable Solid-Fluid Interaction Problems,” Proceedings of the 7th Asia-Pacific Congress on Computational Mechanics (APCOM, Taipei), (2019).

[22] Koji Nishiguchi, Tokimasa Shimada, Rahul Bale, Shigenobu Okazawa, Makoto Tsubokura, “Particle-In-Cell Method using Hierarchical Cartesian Mesh for Deformable Solid-Fluid Interaction Problems,” Proceedings of VIII International Conference on Coupled Problems in Science and Engineering, 1 page, Sitges (Spain), (2019).

[23] Shunpei Oyama, Keizo Yamamoto, Hiromasa Kajimoto, Rahul Bale, Jun Ikeda, Makoto Tsubokura, “Unsteady aerodynamics simulation for the influence of difference in posture change on aerodynamics and flight distance in ski jump take-off motion,” JSME Symposium : Sports engineering and Human Dynamics, B-2, (2019).

[24] HsuehJui Lu, ChungGang Li, Akiyoshi Iida, Tsukasa Yoshinaga, Kazunori Nozaki, Makoto Tsubokura, “A framework for simulation of sibilant fricatives using implicit compressible flow solver,” The 72nd Annual Meeting of the American Physical Society’s Division of Fluid Dynamics (APSDFD)(Nov 23-26 2019, Seattle), C29.00005, (2019).

[25] HsuehJui Lu, ChungGang Li, Makoto Tsubokura, “The Simulation of Flow and Acoustics for Human Phonation System Using Implicit Compressible Flow Solver,” International Conference on Flow Dynamics(ICFD)(Nov 6-8 2019, Sendai), OS12-8, (2019).

13.5.6 Software

13.5.7 Patents